A dual involvement of Protocadherin 18a in stromal cell development guides the formation of a functional hematopoietic niche

Anne-Lou Touret, Catherine Vivier, Anne Schmidt, Philippe Herbomel, Emi Murayama

© 2022. Published by The Company of Biologists Ltd | Development (2022) 149, dev200278. doi:10.1242/dev.200278

RESEARCH ARTICLE

A dual involvement of Protocadherin 18a in stromal cell development guides the formation of a functional hematopoietic niche

Anne-Lou Touret[1,2,3], Catherine Vivier[1,2], Anne Schmidt[1,2], Philippe Herbomel[1,2,*] and Emi Murayama[1,2,4,*]

ABSTRACT

Hematopoietic stem and progenitor cells emerge from the aorta and migrate to the caudal hematopoietic tissue (CHT) of zebrafish larvae, the hematopoietic equivalent of the mammalian fetal liver, for their proliferation and differentiation. We previously reported that somite-derived stromal cells were a key component of the CHT niche. Here, we found that the cell adhesion protein Protocadherin 18a (Pcdh18a) is expressed in the stromal cell progenitors (SCPs) emigrating from somites toward the future CHT. Deletion of most of the Pcdh18a intracellular domain caused a decrease in the number of SCPs, the directionality of their migration, and the cell-contact mediated repulsion that normally occurs between migrating SCPs. These defects were followed by abnormal morphogenesis of the venous plexus that forms the CHT framework, and the inability of the CHT to function as a niche for hematopoietic stem and progenitor cells. Finally, we found that the extracellular domain of Pcdh18a mediates trans heterophilic adhesion of stromal cells to endothelial cells *in vivo* and thereby the reticular versus perivascular fate of SCPs. Thus, Pcdh18a expression in SCPs is essential for the proper development of the hematopoietic niche.

KEY WORDS: Hematopoietic niche, Stromal cells, Cell migration, Protocadherin, Somite, Zebrafish

INTRODUCTION

In vertebrates, hematopoiesis occurs throughout life from hematopoietic stem and progenitor cells (HSPCs) in dedicated niches, such as the bone marrow in adult tetrapods. Such niches are typically structured by two kinds of cells, vascular endothelial cells and mesenchymal stromal cells, among which several subtypes have been discerned (reviewed by Gao et al., 2018). Developmentally, the definitive hematopoietic stem cells arise from the embryo's aorta, and then migrate to their first niche, the fetal liver in mammals, in which they undergo expansion and differentiation into all hematopoietic cell types. Then they migrate to the bone marrow to establish lifelong hematopoiesis. Adult adult-type hematopoiesis in fish takes place in the kidney marrow; we found that in fish larvae the aorta-derived definitive HSPCs first home to a dedicated niche in the tail, which we named the caudal hematopoietic tissue (CHT), which acts as the hematopoietic homolog of the fetal liver in mammals (Murayama et al., 2006). We found that the CHT niche consists in two main components, blood vessels – namely the caudal venous plexus (CVP) – and stromal cells, that interconnect the vascular segments of the CVP. More recently, we found that these stromal cells arise from cell clusters formed within the ventral side of the caudal somites, which undergo an epithelial-mesenchymal transition (EMT) and migrate ventralwards into the presumptive CHT (Murayama et al., 2015). When the maturation of these stromal cell progenitors (SCPs) is impaired, the formation of the CHT niche is affected, resulting in failure to maintain HSPCs and support definitive hematopoiesis (Murayama et al., 2015). At the same time and in the same area, endothelial cells also migrate ventralwards from the primordial caudal vein to form the caudal venous plexus through sprouting angiogenesis (Wakayama et al., 2015). Previously, we reported that the migration of SCPs and vascular endothelial cells during CVP formation seemed to be synchronized, but the molecular mechanisms were not known (Murayama et al., 2015).

Protocadherins (Pcdhs) are cell adhesion molecules that comprise the largest family of proteins within the cadherin superfamily and are subdivided into clustered and non-clustered Pcdhs. The non-clustered Pcdhs are evolutionarily conserved and vary in their regional pattern of expression, prominently within the nervous system (Vanhalst et al., 2005). They further divide into δ1 and δ2 subfamilies based on differences in the number of extracellular cadherin (EC) repeats as well as in the intracellular domain (ICD) (Redies et al., 2005). δ2-Pcdhs comprise Pcdh8, Pcdh10, Pcdh17, Pcdh18 and Pcdh19, they have six EC repeats, and their ICD bears two conserved motifs (CM1 and CM2) (Vanhalst et al., 2005). δ-Pcdhs seem to mediate homophilic cell-cell interactions, although binding appears to be weaker than that of classical cadherins (Harrison et al., 2020; Tai et al., 2010). In addition, δ2-Pcdhs have been shown to mediate heterophilic *cis* interactions with classical cadherins (Biswas et al., 2010; Chen et al., 2009; Kraft et al., 2012). It is still not established whether they can engage heterophilic *trans* interactions. Pcdh17 and Pcdh19 carry a conserved RGD motif in their extracellular domain (EC2), suggesting that they may interact with integrins (Jontes, 2016), but an actual molecular interaction has yet to be demonstrated. Some Pcdhs have been reported to be involved in the fine tuning of adhesion versus repulsion. For example, a deletion of the ICD of Pcdh17 led to a defect in cellular repulsion, resulting in axonal clumping of abducens motor neurons (Asakawa and Kawakami, 2018). The ICD of Pcdhs is known to activate downstream signaling cascades (Pancho et al., 2020). Several Pcdhs are involved in the regulation of actin cytoskeletal dynamics through the WAVE regulatory complex (WRC), and the WRC interacting receptor sequence (WIRS) is highly conserved

[1]Institut Pasteur, Department of Developmental & Stem Cell Biology, Paris 75015, France. [2]CNRS, UMR3738, Paris 75015, France. [3]Sorbonne Université, Ecole Doctorale Complexité du Vivant, Paris 75005, France. [4]INSERM, Paris 75013, France.

*Authors for correspondence (herbomel@pasteur.fr; emur@pasteur.fr)

A.-L.T., 0000-0002-3114-7991; P.H., 0000-0002-8946-3313; E.M., 0000-0002-5311-1594

Handling Editor: Hanna Mikkola
Received 20 October 2021; Accepted 18 August 2022

Development (2022) 149, dev200278. doi:10.1242/dev.200278

among Pcdhs of the δ2 subfamily (Chen et al., 2014). Furthermore, Pcdh18 was identified as a binding partner for Disabled-1 (Dab1), a component of the Reelin signaling pathway that mediates neuronal migration during cortical lamination (Homayouni et al., 2001). Several studies reported that the downstream effectors of the non-clustered Pcdhs are involved in cell movements and motility (Nakao et al., 2008; Biswas et al., 2014; Hayashi et al., 2014).

Here, we report the identification of Pcdh18a as a molecule that is continuously expressed in the SCPs during their emergence and migration in zebrafish embryos and is essential for the formation of a functional hematopoietic niche. Pcdh18a affects the migration of SCPs, notably the repulsion among leader cells, the number of SCPs, and their interactions with endothelial cells, the other main component of the CHT niche. It mediates stromal cell interaction with the endothelium, and thereby conditions the subsequent differentiation fate of SCPs.

RESULTS

Somite-derived SCPs migrate alongside vascular endothelial cells

We previously reported that cell clusters containing SCPs appeared at the ventral side of caudal somites from 21 to 22 hours post-fertilization (hpf) (Murayama et al., 2015). Somites are formed one by one every 30 min in a rostro-caudal direction, and then progressively mature (Stickney et al., 2000). They initially display an epithelial structure on their entire surface; then, cell clusters consisting of about 15-20 cells per somite become apparent on the ventral side, and from these clusters the SCPs soon emigrate as strings in ventral direction (Murayama et al., 2015). At about the same time, vascular endothelial cells sprout from the primordial caudal vein (PV) at the midline and migrate ventralwards together with the SCPs. To examine the spatiotemporal migration path of SCPs in the caudal region relative to endothelial cells, we first performed live imaging using Tg*(pax3a:GFP; kdrl:ras-mCherry)* or Tg*(ET37:GFP; kdrl:ras-mCherry)* double-transgenic embryos. The pax3a:GFP and ET37:GFP transgenes are initially expressed weakly throughout the somites, then pax3a:GFP becomes more strongly expressed in the lateral and ventral cell layers (Lee et al., 2013), which comprise the SCP clusters; then, both transgenes are well expressed in the emigrating SCPs. The kdrl:mCherry transgene specifically labels endothelial cells. Confocal time-lapse imaging of the caudal region of double-transgenic embryos in lateral view followed by digital reconstruction of transverse sections revealed that by 23-25 hpf SCPs that delaminated from the somites then migrated ventralwards on the outer surface of the PV (Fig. 1Aa,Ab, Movie 1). By 27 hpf, they migrated further ventrally together with endothelial cells extending from the ventral wall of the PV (Fig. 1Ba, Movie 1), which by 36 hpf had fully organized into a functional caudal venous plexus (CVP), including the definitive caudal vein (CV) as its ventral-most segment (Fig. 1Ac,Ad). Meanwhile, SCPs/stromal cells (SCs) had settled in between the vascular segments of the CVP, and some of them had migrated further ventrally into the caudal fin to become fin mesenchymal cells (FMCs) (Lee et al., 2013) (Fig. 1Ac,Ad, purple arrows). *In vivo* imaging at higher magnification revealed that during CVP morphogenesis migrating SCPs and vascular endothelial cells dynamically stretched out filopodia through which they interacted (Fig. 1Bb-Bd), then endothelial cells appeared to join and form new lumenized vascular segments around the neighboring SCPs (Movie 1).

To investigate further the morphodynamics of migrating SCPs, we switched to a new transgenic driver line created by us (E.M., C.V., A.S., A.-L.T., P.H., unpublished), TgBAC*(cspg4:GAL4)*, which drives specific expression of Gal4 in SCPs and SCs in addition to the notochord, and we combined it with a Tg*(UAS:Lifeact-GFP)* reporter line in which Lifeact-eGFP highlights F-actin dynamics *in vivo*. SCPs migrating on the outer surface of the PV and further ventrally extended filopodia toward their leading edge and in many other directions, and formed an extensive interconnected network (Fig. 1C, Movie 2).

The cytoplasmic domain of Pcdh18a is involved in stromal cell progenitor migration

To understand the molecular mechanism of SCP emigration from the somites, we performed whole-mount *in situ* hybridization (WISH) analysis for genes encoding cell adhesion molecules, generally involved in cell migration, during SCP emergence in the caudal somites and the ensuing migration period. We found no cadherin expression specifically in the somite ventral clusters/SCPs (see also the zebrafish gene expression library at zfin.org/action/expression/search), so we moved to the protocadherin family. We found that *pcdh18a*, encoding Protocadherin 18a, was expressed in developing SCPs (Fig. 2A). *pcdh18a* expression was first observed in the SCP clusters at the ventral side of caudal somites (Fig. S1A,A′), then also in the migrating SCPs derived from them (Fig. S1B,B′), until at least 35 hpf (Fig. S1C,C′).

To investigate the possible involvement of Pcdh18a in SCP emigration from the somites, we first used an antisense morpholino (MO). Previous studies found that MOs blocking Pcdh18a translation caused defects in the early development of zebrafish embryos and lethality by mid-somitogenesis (Aamar and Dawid, 2008; Bosze et al., 2020). We found that a splice-blocking MO targeting the intron 1-exon 2 (i1e2) junction of nascent *pcdh18a* RNA led with high efficiency to retention of intron 1 in the mRNA (Fig. 2Ba, Fig. S2), resulting in a frameshift past codon 734 and a premature termination codon 13 codons downstream, hence generating a protein retaining only 106 out of the 399 amino acids of its cytoplasmic domain (Fig. 2Bb, Fig. S2C). We named this truncated protein Pcdh18a-ΔCP_{106} (Fig. 2Bb). The cytoplasmic domain deleted by the i1e2 MO notably contains the WIRS peptide (Chen et al., 2014), which is involved in the regulation of F-actin, and the Dab1-interacting domain (Homayouni et al., 2001), which may regulate a tyrosine kinase pathway (Fig. 2Bb), both of which are highly similar to human orthologs (Fig. 2Bc). Following injection of this MO at the one-cell stage, the resulting embryos and swimming larvae displayed a globally normal morphology (Fig. S2D). We then injected this MO in Tg*(pax3a:GFP; TCF:nls-mCherry)* embryos, in which somite-derived SCPs are labeled with GFP and cells of somitic origin with nuclear mCherry (Murayama et al., 2015). By 24-30 hpf, we observed delamination and emigration of SCPs from the ventral side of caudal somites in both control and morphant embryos (Fig. 2C). We then examined how the truncation of the cytoplasmic domain of Pcdh18a occurring in the morphants affected SCP migration. We focused our analysis on the leader cells of the strings of SCPs that emigrate from each caudal somite. We found that the SCP leader cells in pcdh18a-ΔCP_{106} morphants showed a zigzag-like migration pattern (Fig. 2Da-Dc), and, as a result, the straightness of their trajectories was diminished (Fig. 2Dd). Their speed was also affected. We found indeed that the migration of leader SCPs in wild-type (WT) embryos can be divided into two phases: a first phase of fast movement lasting about 90 min, followed by a short rest and then a relatively slow second phase (Fig. 2Ea). This velocity change probably corresponds to the transition from migration on the primordial vein

Development (2022) 149, dev200278. doi:10.1242/dev.200278

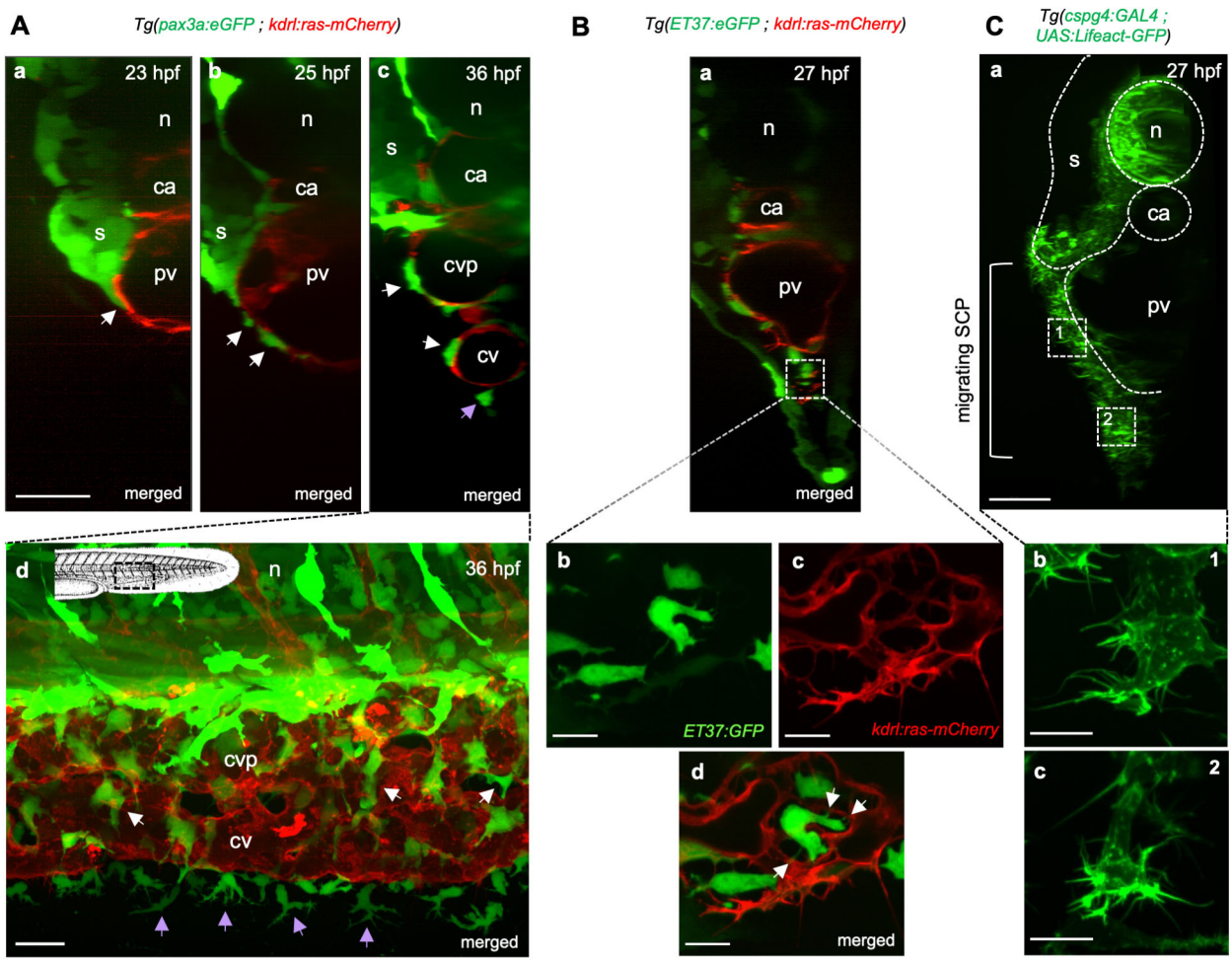

Fig. 1. Stromal-endothelial cell interactions during SCP migration and caudal vein plexus formation. (A-C) Confocal spinning-disk images of live embryos of the indicated transgenic backgrounds and developmental stages. (Aa-Ac) Optical transverse sections reconstituted by Imaris software. White arrows indicate SCPs migrating on the primordial vein or within the forming CVP; purple arrow indicates an FMC. Scale bar: 30 µm. (Ad) Lateral view. Schematic indicates the region shown. GFP^{high} and GFP^{dim} cells are neural crest-derived pigment cells and SCP derivatives, respectively. Scale bar: 20 µm. (Ba) Optical transverse section. (Bb-Bd) Magnified projections from three confocal planes spaced by 0.6 µm at the region indicated by the dashed square in (Ba), ventral to the primordial vein, where angiogenesis is building the CVP. White arrows point to stromal cell interaction with endothelial cells via filopodia. Scale bars: 10 µm. (Ca) Optical transverse section. SCPs first migrate in a 2D mode in close contact with the primordial vein (dashed square marked 1) then in a more 3D mode when they co-migrate with endothelial cells (dashed square marked 2). Scale bar: 20 µm. (Cb,Cc) Magnified images of SCPs in 2D (Cb) and 3D (Cc) migration modes. Scale bars: 10 µm. ca, caudal artery; cv, caudal vein; cvp, caudal vein plexus; n, notochord; pv, primordial vein; s, somites.

surface to a movement in the 3D extracellular matrix (ECM) further ventrally, synchronized with the migration of and interconnection with endothelial cells in the process of forming the venous plexus (Fig. 1). In contrast, SCP leader cells in morphant embryos migrated at a slower, relatively uniform speed without going through these phases (Fig. 2Ea,Eb). In addition, in the *pcdh18a* morphants, migrating SCPs frequently showed a more elongated cell body and thick cellular projections in several directions (Fig. 2Ce,Cf).

To analyze further the migration behavior of SCP leader cells in pcdh18a-ΔCP_{106} morphants, we crossed the TgBAC*(cspg4:GAL4)* line with Tg*(UAS:Lifeact-eGFP)* in order to visualize actin dynamics and cellular projections during SCP migration. In the control group, a high-intensity GFP signal was observed in leader cells mainly near the front of the cell, relative to the direction of cell migration (Fig. 3Aa-Ad, dashed arrows, Movie 3). In contrast, in pcdh18a-ΔCP_{106} morphants, cellular projections were more frequently detected towards the opposite direction (Fig. 3Ae-Ah, B). Quantitative analysis confirmed that, compared with control embryos, leader cells in *pcdh18a* morphants displayed a similar total number of filopodia (mean=11/cell), as well as filopodia growing towards the direction of migration, but 70% more filopodia than controls growing towards the opposite direction (Fig. 3C).

Next, we focused on the features of cell-cell junctions between leader cells and their followers in the SCP strings emigrating from the somites. At the beginning of their migration in control embryos, the leader cells of neighboring strings sometimes contacted each other via filopodia, but these interactions were transient, and they did not affect the direction of migration of the involved cells (Fig. 3Da-Dc). In contrast, in pcdh18a-ΔCP_{106} morphants, when such contacts occurred, they lasted longer, with a resulting change of migration direction of at least one of the two cells (Fig. 3Dd-Df), a behavior that may contribute to the reduced straightness of leader cell trajectories in morphants that we found, as described above (Fig. 2D). In addition, whereas in WT embryos the leader SCPs tended to separate within the first few hours from the follower SCPs, in pcdh18a-ΔCP_{106} morphants leader cells did not easily separate from follower cells during their migration (Fig. 3E, arrows). Among

Development (2022) 149, dev200278. doi:10.1242/dev.200278

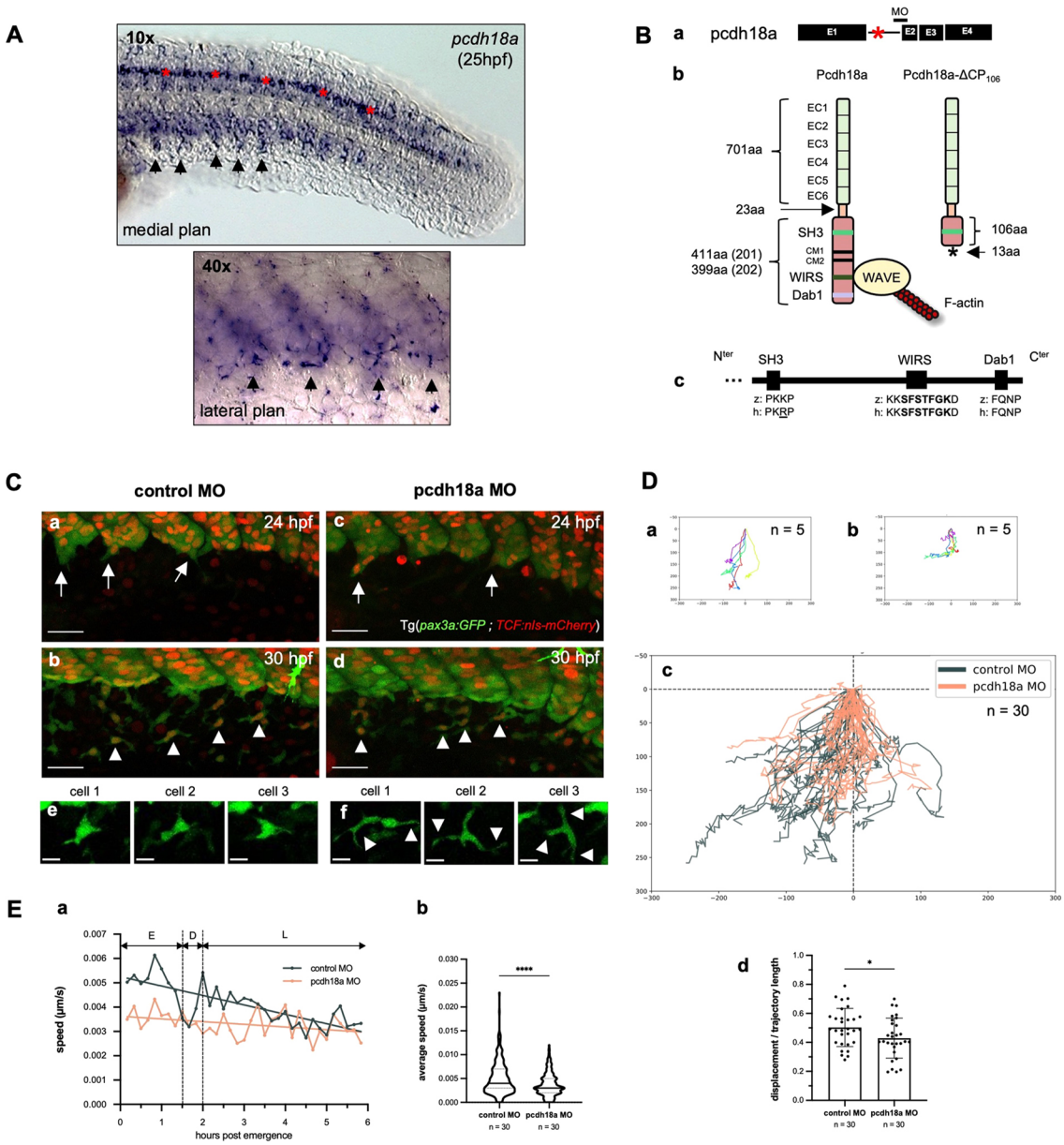

Fig. 2. Pcdh18a is involved in the migration of SCPs. (A) VE-DIC microscopy of whole-mount *in situ* hybridization for *pcdh18a* at 25 hpf. Arrows point to *pcdh18a*-expressing cells at the ventral side of caudal somites, including emigrating SCPs. Some spinal cord neurons are also labeled (red asterisks). The dashed square delimits the region enlarged below. (Ba) The splice-blocking MO used in this study targets the intron 1-exon (E) 2 junction of *pcdh18a*. Asterisk indicates the intron retained in the morphant. (Bb) Injection of this MO leads to retention of the first intron and a premature STOP codon in it, resulting in a protein truncated after the 106th amino acid of the ICD of Pcdh18a. (Bc) Alignment of SH3, WIRS and Dab1 domains in the ICD of human (h) PCDH18 and zebrafish (z) Pcdh18a. (Ca-Cd) Time-lapse confocal imaging of Tg(*pax3a:GFP; TCF:nls-mCherry)* control or pcdh18a-ΔCP_{106} morphant embryos (maximum projections). Arrows and arrowheads indicate delaminating and migrating SCPs/SCs, respectively. Scale bars: 30 µm. (e,f) Snapshots of single SCPs during mid-migration (26-29 hpf). Scale bars: 10 µm. (Da,Db) Individual tracks of five leader SCPs from a control (Da) and a pcdh18a-ΔCP_{106} morphant embryo (Db); cell positions plotted every 10 min over 6 h; *x*,*y* coordinates of the SCPs' starting points (within the somite ventral clusters) are set to (0,0), and negative or positive values on the *x*-axis indicate anterior or posterior migration, respectively. (Dc) Overlay of individual tracks of the 30 leader cells followed in control (black) and pcdh18a-ΔCP_{106} morphant (orange) embryos. n_{exp}=3, $n_{embryos}$=6 for controls and morphants. (Dd) Trajectory straightness of the tracked leader SCPs (mean±s.d.; **P*=0.038; unpaired, two-tailed Student's *t*-test). (Ea) Average speed of the tracked leader SCPs over time. E, early migration; D, decision phase; L, late migration. (Eb) Violin plot of the speed of leader SCPs during their early migration (median±s.d.; *****P*<0.0001; Mann–Whitney test).

the 12 embryos analyzed by 27 hpf, we found 18 leader cells with a long (>10 µm) connection to the follower cells, and only four leader cells with such a long connection in the controls. In addition, these long connections had an almost twofold longer mean duration in the morphants (4 h 50 min versus 2 h 40 min; Fig. 3F). Finally, when the connection eventually broke up, it took much more time to retract back to the cell in the morphants (Movie 4).

Pcdh18a cytoplasmic domain truncation causes a reduction in stromal cell numbers

We next examined whether the absence of most of the cytoplasmic domain of Pcdh18a affected the number of SCPs and their progeny. We counted cells at 26 and 36 hpf, corresponding to the early and latest stages of SCP migration, and at 50 hpf, i.e. once SCs have settled and differentiated within the venous plexus. We found no

Development (2022) 149, dev200278. doi:10.1242/dev.200278

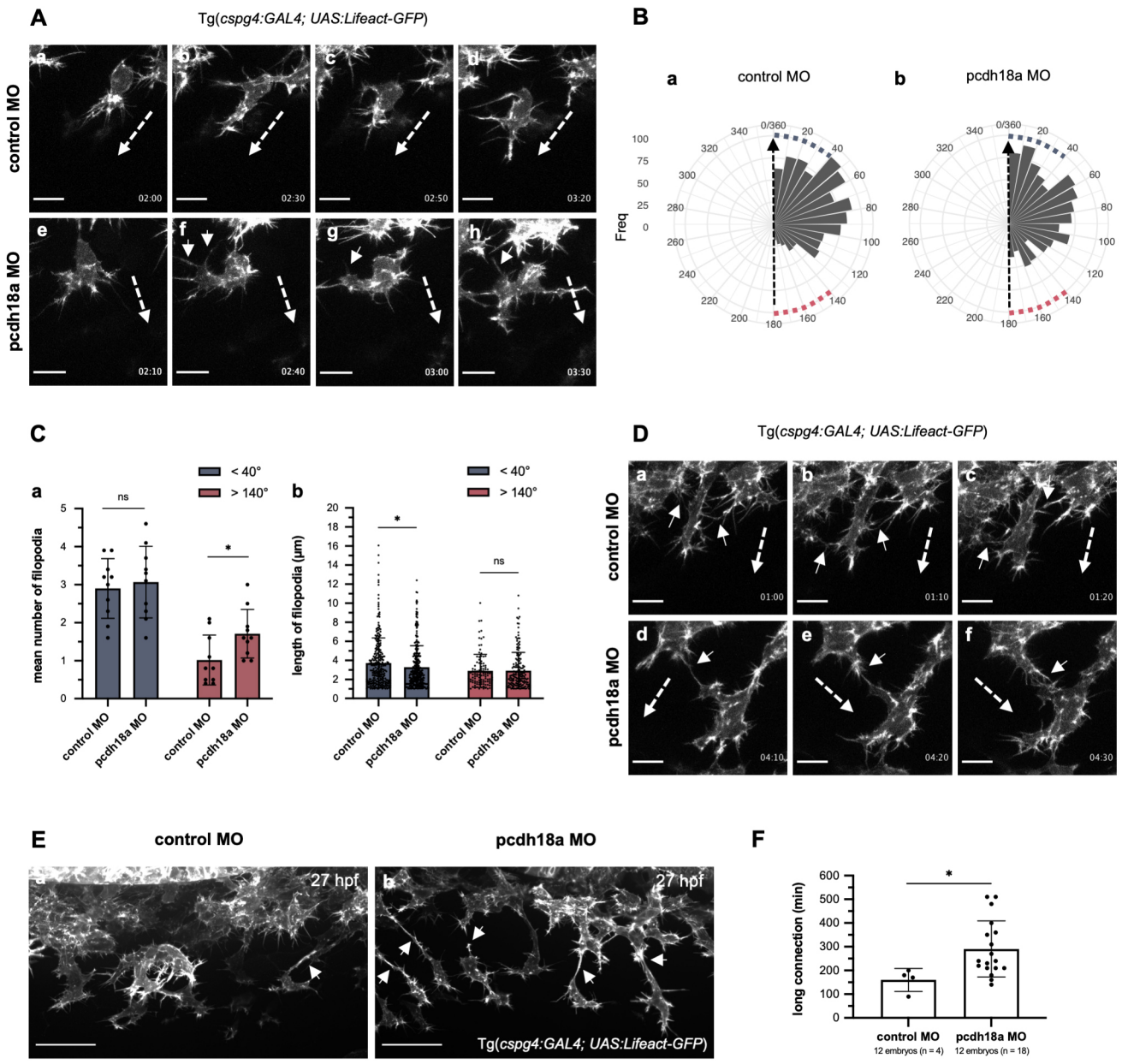

Fig. 3. Pcdh18a modulates cell protrusions and connections of migrating SCPs. (Aa-Ah) Time-lapse confocal images of migrating SCP leader cells from control and pcdh18a-ΔCP_{106} morphant Tg*(cspg4:GAL4; UAS:Lifeact-GFP)* embryos by 26 hpf (see also Movie 3), extracted at 20-30 min intervals. Time from initiation of SCP migration is shown in the lower right of each panel. Dashed and short arrows indicate the direction of SCP migration and filopodia extending in the opposite direction, respectively. Scale bars: 10 µm. (Ba,Bb) Quantification of the frequency of filopodia according to their angle relative to the direction of migration (dashed arrow) in control (Ba) and pcdh18a-ΔCP_{106} (Bb) morphant embryos. Angles <40° and >140° were considered close to the direction of the migration (blue squares) and opposite to the direction of migration (red squares), respectively. The linear mixed-effect model indicates that pcdh18a-ΔCP_{106} morphants have relative angles increased on average by 14.9° compared with controls (P=0.0041). (Ca) Quantification of the mean number of filopodia in sense (<40°, blue) or opposite direction (>140°, red) projected from migrating SCPs in control and pcdh18a-ΔCP_{106} morphant embryos. Each dot represents a biological replicate from five independent experiments (n=10 for controls and morphants) (mean±s.d.; ns, P=0.6666; *P=0.0284; unpaired, two-tailed Student's t-test). (Cb) Quantification of the length of filopodia in the sense (blue) or opposite (red) direction of cell migration. Each dot represents a single filopodium (n=392 for controls, 478 for pcdh18a morphants; mean±s.d.; ns, P=0.5190; *P=0.0247; Mann–Whitney test). (Da-Df) Time-lapse confocal images of migrating leader SCPs from control and morphant Tg*(cspg4:GAL4; UAS:Lifeact-GFP)* embryos around 25-28 hpf, extracted at 10 min intervals. In controls, neighboring leader cells interact by brief contact of their filopodia (Da-Dc, arrows), which do not change their direction of migration (dashed arrows), whereas in morphants they tend to have longer contacts (Dd-Df, arrows), which can change their trajectory. Scale bars: 10 µm. (Ea,Eb) Confocal spinning-disk images of live Tg*(cspg4:GAL4; UAS:Lifeact-GFP)* embryos at 27 hpf. Leader cells tend to show longer connections to follower cells (arrows) in morphants (Eb) compared with controls (Ea). Scale bars: 30 µm. (F) Quantification of the duration of long (>10 µm) cell connections between leader and follower cells (mean±s.d.; *P=0.0113; Mann–Whitney test). See also Movie 4.

difference at 26 hpf, but a nearly 2-fold lower stromal cell number in pcdh18a-ΔCP_{106} morphants by 36 hpf and 50 hpf relative to control embryos (Fig. 4A). We therefore quantified the frequency of cell divisions of SCPs/SCs during their migration (24-36 hpf) and settlement/maturation (36-46 hpf) phases, using time-lapse confocal imaging over these two developmental time windows.

Development (2022) 149, dev200278. doi:10.1242/dev.200278

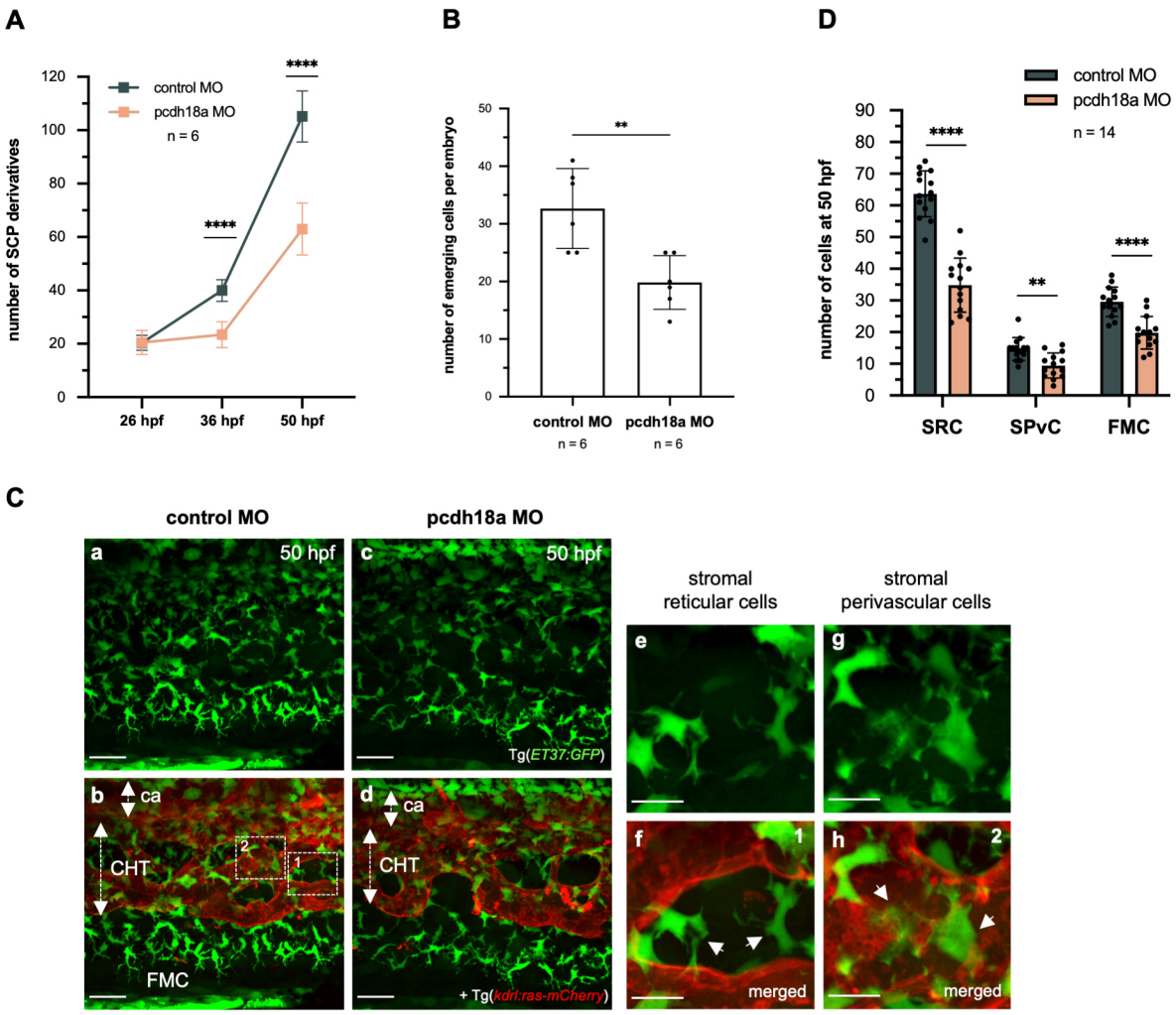

Fig. 4. Pcdh18a C-terminal truncation reduces the number of stromal cells. (A) Counting of ET37:GFP^{+} SCP derivatives in the developing ventral tail over a five-somite width at 26, 36 and 50 hpf. Plots represent biological replicates from a single experiment; n=6 for control and pcdh18a-ΔCP_{106} morphants (mean±s.d.; ****P<0.0001; unpaired, two-tailed Student's t-test). (B) Counts of the number of emerging SCPs within a five-somite width, from 24 to 40 hpf (from the same time-lapse confocal sequences as in Fig. 2C), n=6 embryos per condition (mean±s.d.; **P=0.0037; unpaired, two-tailed Student's t-test). (Ca-Cd) Confocal spinning-disk projections of live Tg*(ET37:GFP; kdrl:ras-mCherry)* control or pcdh18a-ΔCP_{106} embryos at 50 hpf. ca, caudal artery. Scale bars: 30 µm. (Ce-Ch) Dashed boxes in Cb indicate the regions enlarged in Ce-Ch, which show the two stromal cell types found in the CHT at 50 hpf. SRCs interconnect the vascular segments of the plexus and seem to maintain its architecture (Ce, and arrows in Cf), whereas SPvCs are spread along and around the vessels (Cg, and arrows in Ch). Scale bars: 10 µm. (D) Numbers of the three types of SCP derivatives – SRCs and SPvCs in the CHT, and FMCs in the caudal fin – in 14 embryos per condition, counted over a five-somite width (mean±s.d.; **P=0.0011; ****P<0.0001; unpaired, two-tailed Student's t-test).

We found no difference in the number of observed SCP mitoses between control and morphants in the 24-30 hpf and 30-36 hpf intervals (Fig. S3A), and a 2-fold reduction in SCP/SC divisions number in the morphants in the 36-46 hpf interval (Fig. S3B), which matched the nearly 2-fold difference in SCP/SC number at the beginning and end of that time window (Fig. 4A), indicating an actually similar proliferation rate. We therefore quantified the rate of emergence of SCPs from the somites between 26 and 40 hpf, and found a 40% reduction in the morphants (Fig. 4B). We also checked that the reduction in stromal cell numbers in the morphants was not due to apoptosis (Fig. S3C). Thus, the lower final number of stromal cells in pcdh18a-ΔCP_{106} morphants can be mainly ascribed to a lower number of SCP emergence events from the somites.

By 50 hpf, we could identify two subtypes of SCP-derived stromal cells settled in the CHT niche (Fig. 4C): stromal reticular cells (SRCs), which extend cellular projections that interconnect the vascular segments of the venous plexus (Fig. 4Ca,Cb,Ce,Cf), and stromal perivascular cells (SPvCs), which adhere to endothelial cells of the plexus over their entire surface (Fig. 4Ca,Cb,Cg,Ch). We thus compared the numbers of SCP-derived SRCs, SPvCs and FMCs between pcdh18a-ΔCP_{106} morphants and controls. All three cell types showed a similar substantial decrease in the morphants (45% for SRCs, 36% for SPvCs and 33% for FMCs; Fig. 4C,D).

The Pcdh18a cytoplasmic domain conditions stromal cell guidance of venous plexus morphogenesis

We next investigated how truncation of the Pcdh18a cytoplasmic domain affected the behavior of SCPs in relation to the process of venous plexus formation, using time-lapse imaging of Tg*(pax3a: GFP; kdrl:ras-mCherry)* embryos between 26 and 36 hpf (Fig. 5A, Movie 5). Already at 26 hpf, unlike in control embryos (Figs 1 and 5Aa), the migrating SCPs in all examined morphant embryos (n=11) did not appear to adhere to the primordial vein surface (Fig. 5Ab). Later on, in control embryos, SCPs were always present

Development (2022) 149, dev200278. doi:10.1242/dev.200278

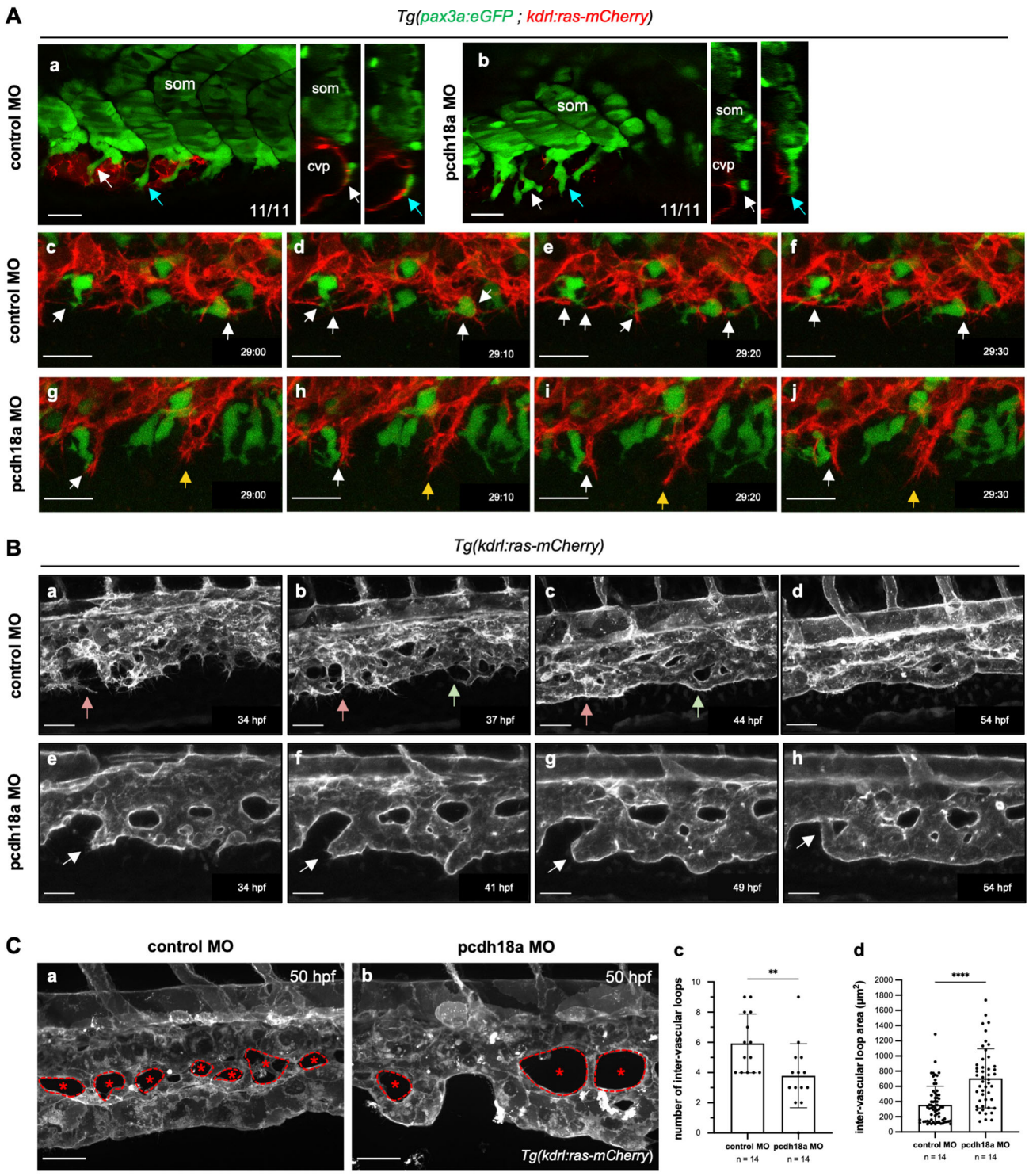

Fig. 5. Pcdh18a truncation impacts on venous plexus morphogenesis. (Aa,Ab) Confocal single-slice images and orthogonal (transverse) views of control (Aa) and pcdh18a (Ab) MO-injected Tg*(pax3a:eGFP; kdrl:ras-mCherry)* embryos at 26 hpf. White and blue arrows point to the same cells (SCPs) shown in transverse view on the right; *n*=11 control and 11 pcdh18a MO-injected embryos, from four independent experiments. cvp, caudal vein plexus; som, somite. (Ac-Aj) Time-lapse confocal imaging of the forming CVP of control (Ac-Af) and pcdh18a-ΔCP$_{106}$ morphant (Ag-Aj) embryos (see also Movie 5). Images were extracted at 10 min intervals from 29 hpf to 29.5 hpf. Dynamic interactions between stromal and endothelial cells (white arrows) were frequent in control embryos whereas in pcdh18a morphants endothelial cells migrated ventralwards apparently regardless of stromal cells (yellow arrows). Scale bars: 20 µm. (Ba-Bh) Time-lapse confocal images from control (Ba-Bd) and pcdh18a (Be-Bh) MO-injected Tg*(kdrl:ras-mCherry)* embryos at later stages (34-54 hpf). See also Movie 6. In the control, red and green arrows follow the formation of new vascular segments. In the morphant, white arrows point to the abnormal tubulogenesis of the definitive caudal vein. Scale bars: 30 µm. (C) Morphological differences in the IVLs. (Ca,Cb) Confocal spinning-disk acquisitions of live transgenic Tg*(kdrl:ras-mCherry)* control or pcdh18a MO-injected embryos at 50 hpf. IVLs are indicated by asterisks and the border of each IVL is delineated by a dashed line. Scale bars: 30 µm. (Cc,Cd) Number (Cc) and surface in µm^2 (Cd) of IVLs over a five-somite width in controls and morphants; *n*=14 embryos per condition, from two independent experiments (mean±s.d.; ***P*=0.0066; *****P*<0.0001; Mann–Whitney test).

Development (2022) 149, dev200278. doi:10.1242/dev.200278

at the forefront of endothelial cells that actively branched and migrated to the ventral side, and they physically interacted with them via cellular projections/filopodia (Fig. 5Ac-Af). In contrast, although both endothelial cells and SCPs migrated to the ventral side in pcdh18a-ΔCP_{106} morphants, they often did not interact (Fig. 5Ag-Aj, Movie 5). In addition, whereas in control embryos SCPs were evenly distributed among migrating endothelial cells, and at some distance from each other (Fig. 5Ac-Af), leading SCPs in morphant embryos were often clustered at the forefront between migrating endothelial cells (Fig. 5Ag-Aj).

We then focused on the subsequent process of venous plexus remodeling (34-54 hpf). Whereas in control embryos, endothelial cells forming the plexus still extended numerous filopodia and projections (Fig. 5Ba-Bd, Movie 6), in the morphants they no longer did so, and rather appeared to have already fused more extensively with each other (Fig. 5Be-Bh, Movie 6). The resulting plexus had fewer branching points compared with controls and tended to show a simpler/flatter structure, with fewer but larger inter-vascular loops (IVLs), and a frequent malformation of the resulting definitive caudal vein, caused by improper fusion events deviating it from its normal course parallel to the body axis (Fig. 5Be-Bh, arrows; 5Ca, Cb). Quantitative analysis confirmed that the number of IVLs was decreased by one-third relative to controls, whereas their mean 2D surface area was increased twofold (Fig. 5Cc,Cd). Finally, imaging at later stages revealed that whereas the WT CHT gradually thins during the process of tail extension (Murayama et al., 2006), this thinning was much more pronounced in the morphants (Fig. 6B).

Pcdh18a cytoplasmic truncation leads to excess deposition of fibronectin in the future hematopoietic niche

Given that truncation of the cytoplasmic domain of Pcdh18a affected not only SCP numbers and migration behavior, but also their interaction with endothelial cells and the final structure of the venous plexus, we speculated that, in addition to a possibly direct involvement of Pcdh18a in these processes, there may be other factors affected by Pcdh18a truncation that may act on both SCPs and vascular endothelial cells in terms of their interactions during venous plexus morphogenesis. Therefore, we looked for genes encoding ECM molecules expressed in the venous plexus area during its formation (24-36 hpf). qPCR analysis of *syndecan 2*,

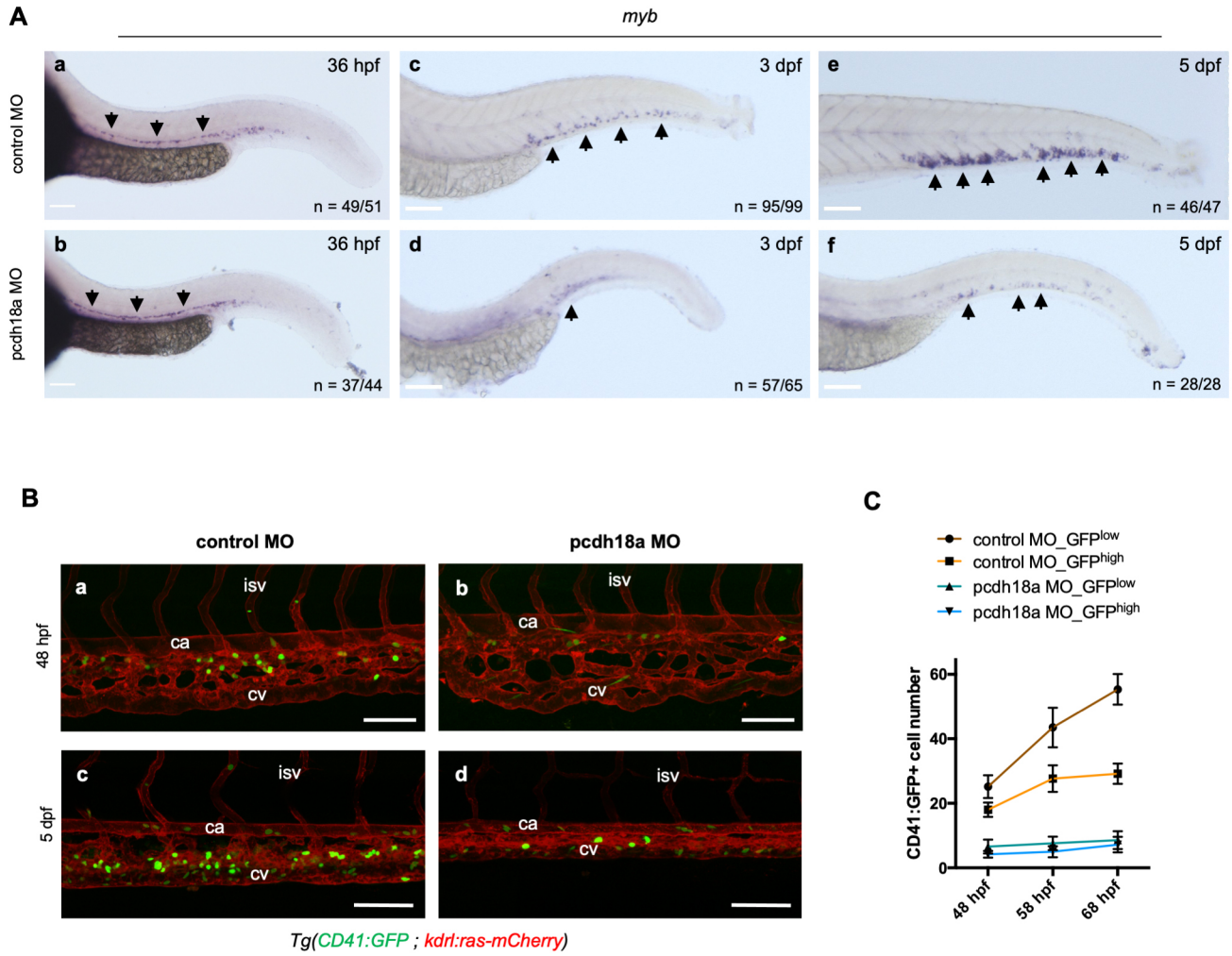

Fig. 6. The Pcdh18a cytoplasmic domain is required for HSPC lodgment and expansion in the CHT. (A) Whole-mount *in situ* hybridization for *myb* expression on control or pcdh18a-ΔCP_{106} morphant embryos at the indicated developmental stages. Arrows indicate *myb*-expressing cells. (Ba-Bd) Confocal maximum projections of control or pcdh18a MO-injected Tg*(CD41:GFP; kdrl:ras-mCherry)* embryos at 48 hpf (Ba,Bb) and larvae at 5 dpf (Bc,Bd). ca, caudal artery; cv, caudal vein; isv, inter-somitic vessel. (C) Counts of CD41:GFP^{low} HSPCs and CD41:GFP^{high} pro-thrombocytes in the CHT over a nine-somite width at 48, 58 and 68 hpf (*n*=6 and 5 larvae for control and pcdh18a morphants, respectively, pooled from three independent experiments), monitored from time-lapse imaging sequences starting at 48 hpf for 20 h. Scale bars: 100 µm.

Development (2022) 149, dev200278. doi:10.1242/dev.200278

cspg4 (*chondroitin sulfate proteoglycan 4*), *hspg2* (*heparan sulfate proteoglycan 2*), *fn1a* and *fn1b* (*fibronectin 1a* and *1b*) expression in the tails of control and pcdh18a-ΔCP_{106} morphants at 36 hpf revealed that *fn1a* and more so *fn1b* were upregulated in the morphants (Fig. S4A). Immunostaining revealed that fibronectin was highly deposited at somite boundaries and the venous plexus in pcdh18a-ΔCP_{106} morphants (Fig. S4B). Optical transverse sections of pcdh18a-ΔCP_{106} morphants (Fig. S4Bg-Bi) revealed surface labeling of mCherry^{+} endothelial cells by the anti-fibronectin antibody. We then performed WISH analysis to identify the cells that express *fn1b*. We found it expressed in caudal somites by 23 hpf, and strongly upregulated there in pcdh18a-ΔCP_{106} morphants (Fig. S4Ca,Cb). At 26 hpf, specific expression of *fn1b* was observed in the endothelial sprouts that will form the venous plexus of morphant but not control embryos (Fig. S4Cc-Cd′). *fn1b* expression was no longer detected at 36 hpf in the tail of control embryos, but still strongly present in the morphants (Fig. S4Ce,Cf).

Pcdh18a cytoplasmic truncation leads to a non-functional hematopoietic niche

We finally examined the extent to which Pcdh18a cytoplasmic truncation affected the resulting niche function of the CHT for HSPCs. We found that in pcdh18a-ΔCP_{106} morphants, definitive aorta-derived HSPCs expressing *myb* were present in the sub-aortic space of the trunk by 36 hpf in numbers similar to control embryos (Fig. 6Aa,Ab). Yet by 3 days post-fertilization (dpf), and even more so at 5 dpf, only few of them had homed to and/or proliferated in the CHT in the morphants (Fig. 6Ac-Af). We examined this defect in more detail by time-lapse confocal imaging of double-transgenic Tg*(CD41:GFP; kdrl:ras-mCherry)* embryos, in which CD41-GFP^{low} cells are HSPCs and CD41-GFP^{high} cells in the CHT are pro-thrombocytes that differentiated from these HSPCs (Kissa et al., 2008) (Fig. 6B). Already at 48 hpf (the peak time of HSPC emergence from the aorta in the trunk), the CHT of morphants had much fewer HSPCs and pro-thrombocytes than controls (Fig. 6C), and this was not a result of cell death among the incoming HSPCs (Fig. S5), indicating a defect in the homing of HSPCs to the CHT. The time-lapse imaging and tracking of cells within the CHT indicated that whereas HSPCs in controls initially homed to the dorsal part of the CHT, and then progressively spread more ventrally, HSPCs in morphants also initially homed dorsally, but then remained in that area (Movie 7). The deficit in HSPCs in the morphant CHT only became more pronounced over time (Fig. 6B, C). Finally, as injection of some morpholinos has been shown to induce the p53 (Tp53) pathway, leading in turn to phenotypic traits as a result of p53 activation (Plaster et al., 2006; Robu et al., 2007), we checked that co-injection of a standard p53 MO with our *pcdh18a* MO led to the same defects in CV plexus structure and HSPC homing in the CHT as the *pcdh18a* MO alone (Fig. S5B).

A *pcdh18a* crispant reproduces the phenotype of pcdh18a-ΔCP_{106} morphants

We then investigated whether the application of CRISPR/Cas9 technology could reproduce the *pcdh18a* mRNA modification and resulting phenotype caused by our *pcdh18a* MO. Single guide RNAs (sgRNAs) were designed to target the area around intron 1 of the *pcdh18a* gene, and we found one that induced at high frequency (~50%) a deletion of 3 bp at the 3′ end of exon 1, and the subsequent retention of intron 1 in the mRNA (Fig. S6A). In ~50% of injected embryos, we observed at 48 hpf morphological abnormalities in the CVP similar to those of *pcdh18a* morphants (Fig. S6B). We next quantified the number of stromal cells and HSPCs by live imaging individual injected embryos that we then genetically checked for the targeted mutation. Both stromal cell and HSPC numbers were reduced in the verified *pcdh18a* crispants relative to control embryos (Fig. S6C,D), thus reproducing the phenotypic traits caused by the *pcdh18a* MO.

Adhesion to endothelium via the extracellular domain of Pcdh18a determines stromal cell subtypes

In addition to cell-cell adhesion through homophilic binding via their extracellular domain (ECD) (Morishita and Yagi, 2007), protocadherins may also engage in heterophilic interactions (Jontes, 2016). We therefore wondered whether the ECD of Pcdh18a might be directly involved in the adhesion of SCPs to vascular endothelial cells. We first searched for cell adhesion motifs, such as RGD, in the ECD of Pcdh18a. Instead of the RGD motif, we found there two REDV motifs, which were originally identified in human plasma fibronectin as a peptide that binds to vascular endothelial cells (Fig. 7Aa). Therefore, we decided to investigate how SCPs behave when a mutation is introduced into the REDV motifs in Pcdh18a. First, to choose the substitution patterns of the four amino acid residues of REDV, we used the SWISS-MODEL server for protein structure prediction to see how various mutations may affect the conformation of the ECD of Pcdh18a. We performed structural predictions for four different substitution patterns – AAAA, AEAV, AEDA and RAAV – and found that the substitution from REDV to AEAV best retained the 3D structure of Pcdh18a, at least under the condition of homophilic interaction (Fig. 7Aa,Ab).

Next, we analyzed the effect of these amino-acid changes *in vivo* by expressing Pcdh18a carrying WT (REDV) or mutant (AEAV) sequences, fused to GFP instead of the Pcdh18a intracellular domain. To overexpress either form specifically in SCPs, we inserted these constructs downstream of a UAS promoter (UAS: pcdh18a-ECD^{REDV}-GFP and UAS:pcdh18a-ECD^{AEAV}-GFP), and injected the resulting plasmids into Tg*(cspg4:Gal4; kdrl:ras-mCherry)* embryos in order to also visualize vascular endothelial cells. We then analyzed the resulting embryos by live confocal imaging at 50 hpf, i.e. when the SCPs have differentiated into stromal cell subtypes. We found that in embryos overexpressing the WT (REDV) Pcdh18a ECD, GFP^{+} stromal cells were mainly of the perivascular subtype, i.e. closely adherent to vascular endothelial cells of the venous plexus (Fig. 7Bc,Bd). In contrast, GFP^{+} stromal cells overexpressing the ECD of Pcdh18a into which the AEAV mutation was introduced were mainly of the reticular type (Fig. 7Be, Bf), and those that were more perivascular displayed a characteristic defect in attachment to the vascular endothelium. They were generally smaller in 2D size than those of control embryos, and only part of the cell adhered to the endothelium (Fig. 7Bg,Bh).

We then counted the proportions of stromal cells of the two subtypes – reticular and perivascular – among GFP^{+} cells overexpressing either the WT or the mutant Pcdh18a ECD form (Fig. 7C). Whereas in normal uninjected embryos the ratio of stromal reticular to perivascular cell number was 80:20 (Fig. 4D), overexpression in stromal cells of the WT Pcdh18a ECD form led to a striking inversion of this ratio, to 20:80, indicating that this overexpression strongly favored the perivascular fate. In striking contrast, overexpression in stromal cells of the mutated (AEAV) Pcdh18a ECD form led to a reticular to perivascular ratio similar to that found in uninjected embryos, i.e. 80:20. Altogether, these qualitative and quantitative results demonstrate that the ECD of Pcdh18a is required for the extensive adhesion of stromal cells to endothelial cells, which characterizes the perivascular subtype, and

Development (2022) 149, dev200278. doi:10.1242/dev.200278

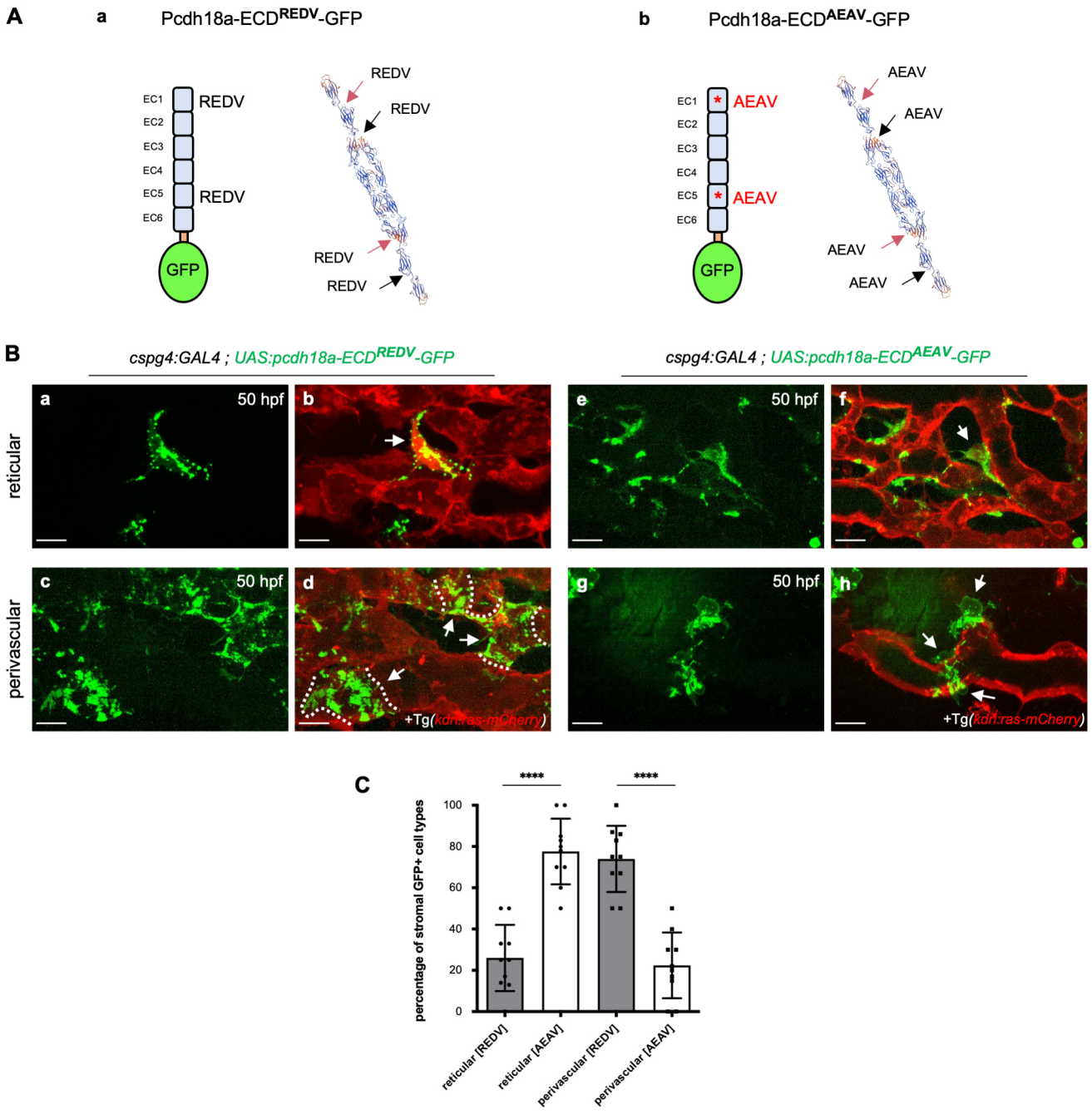

Fig. 7. The extracellular domain of Pcdh18a mediates the adhesion of stromal cells to endothelial cells. (Aa,Ab) Fusion proteins expressed in SCPs via the Gal4/UAS system, with the ICD of Pcdh18a substituted by GFP, and tertiary structure prediction for WT (Aa) and mutant (Ab) forms of the ECD, using SWISS-MODEL (expasy.org). Red and black arrows point to two REDV (WT) or AEAV (mutant) motifs in each of two ECDs in homophilic *trans* interaction. (B) Confocal spinning-disk images of live Tg*(cspg4:GAL4; UAS:pcdh18a-ECD*^{REDV} or ^{AEAV}*-GFP; kdrl:ras-mCherry)* embryos in the CVP at 50 hpf. (Ba-Bd) Pcdh18a-ECD^{REDV}-GFP expressing reticular (Ba,Bb) or perivascular (Bc,Bd) stromal cells (green) overlaid on endothelial cells (red). Dashed lines indicate the border of each SPvC. (Be-Bh) Pcdh18a-ECD^{AEAV}-GFP expressing reticular (Be,Bf) or perivascular (Bg,Bh) stromal cells (green) overlaid on endothelial cells (red). GFP^{+} SPvCs typically showed only partial adherence to the endothelium. Arrows indicate GFP^{+} reticular (Bb,Bf) and perivascular (Bd,Bh) cells, respectively. Scale bars: 10 µm. (C) Histogram showing the percentage of reticular versus perivascular cells among pcdh18a-ECD^{AEAV}-GFP- or pcdh18a-ECD^{REDV}-GFP-expressing stromal cells at 50 hpf. *n*=10 embryos per condition, from a single experiment (mean±s.d.; ****P<0.0001; unpaired, two-tailed Student's *t*-test).

that this effect is strictly dependent on the REDV peptides of the Pcdh18a ECD.

DISCUSSION

SCPs differentiate from zebrafish caudal somites via EMT. The timing of EMT in SCPs during somite development is still uncertain, but SCPs probably remain in the cluster for a while after the EMT, then delaminate ventrally around 23-24 hpf. Mesenchymal cell migration is characterized by cell polarization, forming a leading edge that extends actin-rich protrusions, and subsequent migration by retraction of the contractile rear. Cell migration and adhesions are interdependent processes that influence diverse cellular fates. Neural crest cells (NCCs), a highly motile, EMT-derived cell population, undergo collective cell migration,

Development (2022) 149, dev200278. doi:10.1242/dev.200278

and the involvement of cadherins in this process is well known. Like NCCs, SCPs undergo collective migration, but we call this a 'semi-collective migration' because the number of cells in a group is fewer (two or three cells) than for NCCs. Semi-collective migration of SCPs occurs immediately after delamination from the SCP clusters at the ventral side of somites, and, shortly thereafter, the leader cell releases itself from the follower. This characteristic suggests that binding through cell adhesion molecules among SCPs may be less tight (or more flexible) than that of NCCs. We observed no expression of cadherin genes in the SCPs, suggesting that protocadherins such as Pcdh18a may act as a substitute for cadherins in SCPs. Pcdh18a is indeed expressed in SCPs within the clusters and during their subsequent migration. We found that it facilitates their overall emergence from the clusters over time, as a truncation of its ICD caused a nearly 2-fold reduction in the total number of SCPs that emerged from the somites, and it also promotes their ventralwards navigation, as the latter is less direct when Pcdh18a ICD is truncated. This may be connected to the fact that the truncated Pcdh18a no longer contains the WIRS sequence that can bind the WAVE complex and thereby trigger actin polymerization. We also found that the Pcdh18a ICD is involved in repulsion between leader cells among migrating SCPs. This is reminiscent of previous data relating to two other δ2-Pcdhs. A study based on cell aggregation assays found that Pcdh19 lacking its ICD induced the formation of larger aggregates than did full-length Pcdh19 (Tai et al., 2010). Then, two studies reported repulsive forces among axons (Hayashi et al., 2014), and among abducens motor neurons in zebrafish (Asakawa and Kawakami, 2018), that were dependent on the ICD of Pcdh17. Thus, it appears that the ICD of δ2-Pcdhs can have an adhesion-inhibiting role, although the mechanism is still unknown.

The presence of Pcdhs, which mediate weaker homophilic interactions than cadherins, in migrating SCPs, may help to ensure the flexibility to switch from the collective migration of SCPs to their interaction with vascular endothelial cells in a short time after delaminating from somite clusters. The endothelial cells forming the caudal venous plexus express no Pcdh18, but a variety of integrins (Xue et al., 2019), notably α5β1, which can bind to the RGD motif present on other cells or proteins of the ECM. The ECD of Pcdh18a contains no RGD motif; we found in it two copies of a REDV motif that had been reported to mediate protein binding to endothelium expressing integrin α4β1, and these two motifs were in an exposed position on the predicted 3D structure of Pcdh18a. By expressing a WT or mutated form of Pcdh18a specifically in SCPs/SCs, we demonstrated that the ECD of Pcdh18a is essential, via its REDV motifs, for the adhesion of SCPs/SCs to the CVP endothelium. This is probably the first documented case of *trans* heterophilic binding of a δ2-family protocadherin *in vivo*, and it bears a high biological significance, as it conditions the formation of a functional hematopoietic niche (the CHT). Furthermore, overexpression of Pcdh18a-ECD at the surface of SCPs/SCs strongly favored the installment of SCPs as perivascular rather than reticular stromal cells, which normally largely predominate. It remains to be explored whether this shift is accompanied by actual changes in differentiation at the molecular level.

In addition to its ECD, the ICD of Pcdh18a also appears to be important for the proper interactions of SCPs/SCs and endothelial cells. Indeed, pcdh18a-ΔCP_{106} morphants display morphological defects of the final venous plexus. SCPs may orchestrate the migration and orderly fusion pattern of endothelial cells to form a venous plexus of adequate shape, possibly by preventing them to fuse too rapidly and extensively, as seems to happen in the pcdh18a-ΔCP_{106} morphants. We note that SCPs are distributed evenly among endothelial cells in the process of forming the plexus, thus maximizing the number of endothelial cells in contact with at least one SCP, whereas SCPs are both nearly 2-fold less numerous and less evenly distributed in pcdh18a-ΔCP_{106} morphants, which may compromise this orchestrating function.

We also considered the possibility that changes in the ECM may be involved in the abnormal remodeling of the venous plexus in pcdh18a-ΔCP_{106} morphants. Surprisingly, we found that fibronectin was excessively expressed and accumulated in the CHT of these morphants. WISH analysis showed that *fn1b* expression was markedly elevated in the caudal somites of pcdh18a-ΔCP_{106} morphants by 23 hpf, and then expressed in the caudal vasculature by 26 hpf, unlike in control embryos. This excess accumulation of fibronectin in the caudal region of pcdh18a-ΔCP_{106} morphants may contribute to the observed defects in venous plexus formation. Zebrafish Fibronectin 1b contains no REDV motif, but two RGD motifs and two LDV motifs, which can bind to integrins α5β1 and α4β1 (Komoriya et al., 1991), respectively, and both of these integrins are expressed by endothelial cells forming the venous plexus (Xue et al., 2019). Thus, excess Fibronectin 1b may compete with the binding of SCPs/SCs to endothelial cells of the venous plexus, notably through its LDV motifs, which bind the same α4β1 integrin as the REDV motifs of Pcdh18a-ECD that we found to mediate stromal cell binding to these endothelial cells. It remains unclear why and how a deficiency in the Pcdh18a-ICD causes an increase in expression of the fibronectin genes in caudal somites and endothelial cells. We speculate that unusual cell-cell interactions caused by Pcdh18a truncation in SCPs may induce a microenvironmental stress and promote the secretion of extracellular ECM, notably fibronectin, by nearby cells.

This study adds new insights into the functions of Pcdh18a, as an adhesion molecule that plays an essential role in the development of SCPs, a newly recognized cell model arising from an EMT. After the EMT, SCPs remain in the clusters at the ventral side of somites for a while, then undergo semi-collective cell migration in which two or three cells from a string, but, shortly after, switch binding partners from SCPs to vascular endothelial cells. Pcdh18a is continuously expressed in SCPs during these three steps. Thus, in a different state of cell dynamics in SCPs, Pcdh18a may flexibly regulate the functions of the extracellular and intracellular domains in response to the microenvironment. Substrate selectivity or affinity in mesenchymal cell migration is also a crucial point in the field of cancer research. Cancer cells are known to disseminate in amoeboid, mesenchymal, and collective cell migration modes, which are affected by tumor microenvironment and treatment (Wolf et al., 2003). Recent discussions have raised the possibility that such plasticity of cancer cell migration is a hindrance to certain treatments (reviewed by Wu et al., 2021; Clark and Vignjevic, 2015). Our research contributes to the understanding of cell behavior *in vivo* by analyzing the function of a protein that could be a molecular switch of 'migration modes' affecting cell plasticity during cancer metastasis and tumorigenesis.

MATERIALS AND METHODS

Zebrafish husbandry

Fish maintenance at Institut Pasteur the regulation of the 2010/63 UE European directives. We used several zebrafish transgenic lines, including Tg*(pax3a:eGFP)* (Seger et al., 2011), Tg*(ET37:eGFP)* (Parinov et al., 2004), Tg*(kdrl:ras-mCherry)* (Chi et al., 2008), Tg*(UAS;Lifeact-eGFP)* (Helker et al., 2013), Tg*(cspg4:Gal; UAS:RFP)* (created in our own lab). Embryos were collected and raised at 28°C, or at 24°C, taking in account the

Development (2022) 149, dev200278. doi:10.1242/dev.200278

25% delay in development relative to 28°C, as described (Kimmel et al., 1995). In order to prevent pigmentation, embryos were developed in N-phenylthiourea (PTU, Sigma-Aldrich, P7629) in Volvic source water (0.003% final), supplemented with 280 mg/l Methylene Blue (Sigma-Aldrich, M4159). For experiments, embryos were anesthetized in 1× tricaine (Sigma-Aldrich, A5040), equivalent to a final concentration of 160 µg/ml.

Plasmid constructs

First, we cloned the *pcdh18a* whole sequence in a pG1_Tol2_hsp70 vector, from cDNA made from a pool of 25-36 hpf embryo tails (see 'RNA extraction and cDNA synthesis' section). We separated the gene into four fragments (around 1000 bp each) and amplified them using the Expand High Fidelity Polymerase (Sigma-Aldrich, 11732641001) and primers 1-8 (see Table S1). We used the TA cloning kit (Thermo Fisher Scientific, K202020) to clone the DNA fragments, then the Gibson Assembly strategy (NEB, E2611S) to obtain the whole gene sequence, using primers 9-16 (see Table S1). To generate the UAS:pcdh18aECD$^{REDV/AEAV}$-GFP constructs, we used pG1_Tol2_hsp70:pcdh18a as a template and the Gibson Assembly strategy with the vector Tol2_4xnr_UAS_eGFP and primers 17-20 for the REDV (non-mutated) form and the intermediate primers 21-24 for the AEAV (mutated) form using a PCR-directed mutagenesis approach (see Table S1, mutated sites in bold). The constructs were fully verified by sequencing.

Plasmid and MO injections

Plasmid constructs were purified using the NucleoBond Xtra Midi endotoxin free kit (Macherey Nagel, 740420.10). We co-injected into one-cell-stage zebrafish embryos 15 pg of UAS:pcdh18aDCD$^{REDV/AEAV}$-GFP construct with 25 pg of tol2 transposase mRNA, transcribed from linearized pCS-zT2TP plasmid (Suster et al., 2011) using the mMESSAGE mMACHINE SP6 kit (Ambion, AM1340). Embryos expressing GFP were sorted and imaged at the desired stages.

A splice-blocking MO targeting the intron 1-exon 2 splice junction of *pcdh18a* (5′-TACTGACCCTGATGGAGTATTGAGA-3′) was injected at an amount of 4 ng into one-cell-stage zebrafish embryos. When co-injected with a p53 MO (Robu et al., 2007), 4 ng of each MO were injected. A standard control MO from Gene Tools (5′-CCTCTTACCTCAGTTACAATTTATA-3′) targeting a mutated form of the human β-globin pre-mRNA was injected at the same amount of 4 ng in control embryos. Control and *pcdh18* i1-e2 morphant embryos were picked randomly for fluorescence microscopy.

Whole-mount immunohistochemistry and TUNEL

Dechorionated and anesthetized embryos were fixed at desired stages in 4% methanol-free formaldehyde (FA) (Polysciences, 040181) for 2 h at room temperature and then rinsed in PBSDT [1× PBS, 0.01% DMSO, 0.1% Triton X-100 (Sigma-Aldrich, T9284)] for use within the next few days. The first day, embryos were treated with 0.1% Tween 20 during 30 min at room temperature, then with acetone for 20 min at −20°C, rinsed in 1× HBSS (Invitrogen/Gibco, 14025), supplemented with 0.1% Tween 20, then treated with collagenase (Sigma-Aldrich, C9891) at a final concentration of 1 µg/ml, rinsed in PBSDT and incubated in blocking solution 1× WBR (Roche, 11921673001) for at least 4 h. They were then incubated overnight at 4°C with primary antibodies: chicken anti-GFP (Abcam, ab13970; 1/800), mouse anti-mCherry (Abcam, ab125096; 1/100), rabbit anti-fibronectin (Sigma-Aldrich, F3648; 1/100). On the second day, embryos were rinsed several times in PBSDT and endogenous peroxidase was inactivated by treatment with 6%H_2O_2 (Sigma-Aldrich, H1009) for 30 min. Embryos were then incubated in the blocking solution for at least 4 h and incubated overnight at 4°C with secondary antibodies: goat anti-chicken Alexa Fluor 488 (Invitrogen, A11039; 1/800), goat anti-rabbit HRP (Thermo Fisher Scientific, G-21234; 1/300), goat anti-mouse HRP (Thermo Fisher Scientific, G-21040; 1/300). On the final day, samples were rinsed several times in PBT (PBSDT without DMSO) and treated with 1 M imidazole (Sigma-Aldrich, I5513) in PBT supplemented with H_2O_2, Alexa Fluor 546 Tyramide Reagent (Invitrogen, B40954; 1/200) or Alexa Fluor 647 Tyramide Reagent (Invitrogen, B40958; 1/25). Finally, embryos were treated with DAPI (Thermo Fisher Scientific, 62248) and gradually transferred to 80% glycerol. TUNEL staining was performed using the ApopTag Red In Situ Apoptosis Detection Kit (S7100, Merck Millipore) combined with peroxidase coupled anti-DIG antibody (Roche, 11207733910; 1/200) followed by tyramide-based amplification (Le Guyader et al., 2008).

Whole-mount *in situ* hybridization

Dechorionated and anesthetized embryos were fixed at desired stages in 4% methanol-free FA (Polysciences, 040181) overnight at 4°C and stored in 100% methanol at −20°C. The protocol used is based on that described by Thisse and Thisse (2008). On the first day, embryos were progressively rehydrated in PBT and permeabilized with 10 mg/ml proteinase K (Ambion, AM2546) for 5 min, then refixed in 4% FA for 20 min. Embryos were incubated for at least 4 h at 60°C in pre-hybridization buffer (HB+), then with 200 ng of digoxigenin-labeled probe. Probes were synthetized from a PCR product or a linearized plasmid (see Table S2) with T7 or SP6 RNA polymerase (Promega, P4074 or P4084) in the presence of DIG-UTP nucleotides. On the second day, embryos were rinsed in HB− buffer (HB+ without torula RNA and heparin) supplemented with saline-sodium citrate buffer (SSC; Sigma-Aldrich, S6639) and then transferred gradually to PBT. They were incubated for at least 4 h in blocking solution 1× WBR (Roche, 11921673001) and incubated overnight at 4°C with an anti-digoxigenin antibody coupled to alkaline phosphatase (Roche, 11207733910; 1/4000). On the last day, embryos were rinsed several times in PBT and the staining reaction was performed. Samples were incubated in NTMT buffer (100 mM Tris-HCl, pH 9.5, 50 mM $MgCl_2$, 100 mM NaCl, 0.1% Tween 20) for at least 5 min and then with NBT/BCIP (Sigma-Aldrich, N6639, B-8503) diluted in NTMT buffer. The reaction was stopped by replacing the solution with PBT, and embryos were stored in 80% glycerol. Bright-field images were captured using a ZEISS Axio Zoom.V16 with a 160× zoom.

RNA extraction and cDNA synthesis

We anesthetized embryos and cut their tails just past the yolk extension at desired stages. Batches of ten tails were immediately frozen in liquid nitrogen and stored at −80°C; 30-60 tails were pooled per biological replicate and three biological replicates were used per condition.

For mRNA extraction, we used TRIzol (Invitrogen, 15596026) and lysed tissues by mechanical pipetting. A volume of 1:5 chloroform was added, samples were vortexed and centrifuged at 12,000 ***g*** for 15 min. The aqueous phase was transferred to a new tube and a volume of 1:1 isopropanol was added and samples were incubated 30 min at −20°C and centrifuged at 1000 ***g*** for 30 min. The pellet was rinsed in 75% ethanol and resuspended in RNase-free water. Samples were treated with DNase I (Invitrogen, AM2239), precipitated a second time with GlycoBlue (Invitrogen, AM9515) and centrifuged at 12,000 ***g*** for 30 min. The resulting pellet was rinsed in 70% ethanol, resuspended in RNase-free water and samples were stored at −80°C.

For cDNA synthesis, we used the Super Script IV kit (Thermo Fisher Scientific, 18091200) according to the manufacturer's protocol. We adjusted the amount of RNA used to have the same for each replicate with a maximum amount of 2500 µg RNA. Samples were treated with RNase H for 20 min at 37°C to remove any trace of RNA, and then stored at −20°C.

Quantitative real-time PCR

Total RNA was extracted at 36 hpf from tails of control or *pcdh18a* i1e2 MO-injected embryos. cDNAs were synthetized and diluted at a final concentration of 15 µg/µl for each biological replicate. qPCR was performed using 7.5 µl of Takyon Rox SYBR Master mix blue dTTP kit (Eurogentec, UF-RSMT-B0701), 1.5 µl of cDNA and 0.5 µl of each 5 µM primers (see Table S3). Real-time qPCR was carried out for three biological replicates with measurements taken from three technical replicates on an Applied Biosystems 7300 Real Time PCR system (Thermo Fisher Scientific). After normalization to zebrafish *elongation factor 1a* (*ef1a*), the relative expression of *fn1a* and *fn1b* was determined using the $2^{-\Delta\Delta Ct}$ method.

Development (2022) 149, dev200278. doi:10.1242/dev.200278

Primer efficiency measurement was carried out by diluting a reference batch of cDNA at 5×, 10×, 20×, 40× and performing qPCR as described previously. Calibration curves were obtained with the $2^{-\Delta\Delta Ct}$ method and the formula $10^{(-1/slope)-1)}\times100$ to obtain the efficiency. Only primers with an efficiency of 90-110%, with no amplification in the H_2O negative control, were selected.

Assessment of *pcdh18a* MO specificity and efficiency

To verify that the *pcdh18a* i1e2 MO prevents splicing of the first intron of the *pcdh18a* gene, we performed PCR on cDNA from control or *pcdh18a* MO-injected embryos. We used one primer in exon 1 and one in exon 2 (FP 5′-CAGTCGTCAATCCCTGAACAG-3′ and RP 5′-GCTGCGAGAG-TATTTGTTCCC-3′), or one primer in exon 1 and one in exon 3 (FP 5′-CAGTCGTCAATCCCTGAACAG-3′ and RP 5′-CGCCACGCCCAC-TATCTTTC-3′) and checked that the size of DNA fragments of morphants corresponded to the insertion of intron 1 compared with controls. Sequencing of *pcdh18a* i1e2 morphant cDNA confirmed intron 1 retention.

Generation of *pcdh18a* crispants

To mimic the protein truncation obtained by *pcdh18a* MO, we designed an sgRNA that causes intron 1 retention of the *pcdh18a* gene. Transient CRISPR-Cas9 targeting of the *pcdh18a* gene was performed by using Alt-R CRISPR-Cas9 system [Integrated DNA Technologies (IDT)]. The sgRNA target site (5'- GTAGAGGTAAAAGCTAGATT-3′) was designed and evaluated for off-target sites using the sgRNA design tool (IDT). Alt-R S.p. Cas9 V3 enzyme (IDT) and equimolar amounts of crRNA:tracrRNA duplexes (IDT) were mixed and incubated to form RNP complexes before injection. The mixed solution was diluted with Cas9 buffer (NEB) to adjust the concentration of Cas9 and sgRNA working solutions to 12 and 18 µM, respectively, and 1 nl was injected into the cytoplasm of one-cell-stage Tg*(pax3a:eGFP; kdrl: ras-mCherry)* or Tg*(CD41:GFP; kdrl:ras-mCherry)* embryos. Injected F0 crispant embryos were individually screened by genomic PCR using primers E1-F 5'-GAGCCAACA-CAGTCGTCAATC-3′ and E2-R 5'-GCTGCGAGAGTATTTGTTCCC-3′, which recognize sites adjacent to intron 1 of exons 1 and 3 of the *pcdh18a* gene. For the cDNA analysis of crispants, total RNA was extracted from 40-50 pooled embryos and RT-PCR was performed using the primers described above to check the resulting splicing patterns.

Embryo mounting for confocal imaging

Dechorionated and anesthetized embryos were mounted in a lateral position with their tails in close contact with the bottom of a 35 mm glass-bottom µ-dish (ibidi, 81158). They were embedded in 1× low-melting agarose (Promega, V2111) in 1× tricaine/1× PTU Volvic water, which was also added on top of it after agarose solidification.

In vivo confocal imaging

For *in vivo* live imaging, we used an inverted spinning disk confocal microscope (Andor, Resolution WD, Yokagawa CSU-W1, coupled with a Leica Dmi8 microscope), equipped with 488 nm and 561 nm laser diodes for excitation, two digital CMOS cameras (Hamamatsu ORCA-Flash4.0 LT, 2048×2048 pixels), a 63× water immersion objective (Leica HC PL APO CS2, NA 1.20, WD 300 µm) and MetaMorph acquisition software. Optical planes were spaced by 0.3 µm and laser diode power was set at 10% with exposure time between 100 and 300 ms, depending on the transgenic line used.

For *in vivo* time-lapse imaging, we used an inverted laser scanning confocal microscope (Leica TCS SP8, CTR 6500), equipped with 488 nm and 552 nm lasers for excitation, two PMT and a Hybrid Detector, and a 40× or 20× immersion objective (Leica HC PL APO CS2 NA 1.1, WD 650 µm, and NA 0.75, WD 670 µm, respectively) and LAS X acquisition software. Usually, two controls and two morphants were acquired in parallel every 10 min with optical planes spaced by 1.5 µm.

For immunohistochemistry imaging, we used an inverted scanning confocal microscope (Leica TCS SPE, CTR 6000), equipped with 405 nm, 488 nm, 532 nm and 635 nm lasers for excitation, one PMT detector, a Leica ACS APO 40× oil objective (NA 1.15, WD 270 µm) and LAS X acquisition software. Optical planes were spaced by 0.8 µm.

VE-DIC microscopy

VE-DIC (video-enhanced differential interference contrast microscopy) acquisitions of *in situ* hybridizations were performed using a Polyvar 2 microscope (Reichert) and a tri-CCD HV-D25 analog camera (Hitachi), adjusted to maximize contrast (Herbomel and Levraud, 2005). Embryos were imaged with either a 10× objective (Reichert PlanFIApo, NA 0.30) or a 40× water lens (Olympus), LUMPlanFi, NA: 0.80. Image sequences were recorded on Mini DV digital video tapes (Sony), using a GV-D1000E PAL recorder (Sony), then the selected images were extracted using SwiftCapture software (Ben Software).

Image analysis

For basic image treatment, we used Fiji software (ImageJ) and for 3D visualization we used Imaris software (Bitplane, v8.1). Cell tracking was made by using the manual tracking function of the TrackMate plugin (v.6.0.3) of Fiji and plotted with a Python script written by S. Rigaud (Image Analysis Hub of Institut Pasteur). For filopodia analysis, we used the Filopodyan plugin (v1.2.6) available in Fiji (Urbančič et al., 2017). The cut-off threshold was set to 1 µm. For each condition, ten SCP leader cells were analyzed at ten time points, corresponding to 90 min of cell migration, from confocal time-lapse sequences of Tg*(cspg4:Gal4; UAS:Lifeact-GFP)* embryos injected with control or *pcdh18a* i1e2 MO. For the Filopodyan setup, we used the triangle threshold, two or three ID iterations and 1-3 LoG sigma, allowing detection of the angles of filopodia relative to the imaged field and their length for each cell. The direction of cell migration was derived from the initial and final position of the cell in the analyzed time window, then a Python script written by D. Ershov (Image Analysis Hub, Institut Pasteur) derived the angle of filopodia relative to the direction of cell migration from 0° to 180° and their length.

Statistical analysis

Basic statistical analysis was performed using GraphPad Prism 9 software. To compare control and morphant groups, we first verified whether the data followed a normal distribution by the Shapiro–Wilk test. If it was the case, we used an unpaired, two-tailed Student's *t*-test assuming that both populations had the same s.d.; if not, we used the non-parametric Wilcoxon–Mann–Whitney test. For the homogeneity of the analyses, if one data set followed a normal distribution and the other not, in the same experimental series, we applied the non-parametric test for both.

Filopodyan analysis was performed using a R script written by H. Julienne (Bioinformatics & Biostatistics Hub, Institut Pasteur). Because the same cell is followed across ten time points to get an average of the relative angle for each cell, results are not independent. A linear mixed effect model was implemented to add a random variable effect, allowing the effect of repeated measurements to be modeled for each cell.

Acknowledgements

We thank Stephane Rigaud, Dmitry Ershov and Jean-Yves Tinevez (Image Analysis Hub of Institut Pasteur) and Hannah Julienne (Bioinformatics & Biostatistics Hub of Institut Pasteur) for implementation of Python scripts and an R-script, respectively, which helped us quantify filopodia dynamics and statistics.

Competing interests

The authors declare no competing or financial interests.

Author contributions

Conceptualization: E.M.; Methodology: A.S., E.M.; Validation: A.-L.T., P.H., E.M.; Formal analysis: A.-L.T.; Investigation: A.-L.T., C.V., E.M.; Resources: C.V., P.H., E.M.; Writing - original draft: A.-L.T., P.H., E.M.; Writing - review & editing: A.-L.T., P.H., E.M.; Visualization: A.-L.T.; Supervision: P.H., E.M.; Project administration: E.M.; Funding acquisition: P.H.

Funding

This work was funded by Institut Pasteur and the Centre National de la Recherche Scientifique, and by grants from the Fondation pour la Recherche Médicale (Equipe FRM DEQ20160334881 to P.H.). and the Fondation ARC pour la Recherche sur le

Cancer (to P.H.). A.-L.T.'s fourth year of PhD fellowship was funded by the Agence Nationale de la Recherche Laboratoire d'Excellence Revive (Investissement d'Avenir; ANR-10-LABX-73).

Peer review history

The peer review history is available online at https://journals.biologists.com/dev/lookup/doi/10.1242/dev.200278.reviewer-comments.pdf.

References

Aamar, E. and Dawid, I. B. (2008). Protocadherin-18a has a role in cell adhesion, behavior and migration in zebrafish development. *Dev. Biol.* **318**, 335-346. doi:10.1016/j.ydbio.2008.03.040

Asakawa, K. and Kawakami, K. (2018). Protocadherin-mediated cell repulsion controls the central topography and efferent projections of the abducens nucleus. *Cell Rep.* **24**, 1562-1572. doi:10.1016/j.celrep.2018.07.024

Biswas, S., Emond, M. R. and Jontes, J. D. (2010). Protocadherin-19 and N-cadherin interact to control cell movements during anterior neurulation. *J. Cell Biol.* **191**, 1029-1041. doi:10.1083/jcb.201007008

Biswas, S., Emond, M. R., Duy, P. Q., Hao, L. T., Beattie, C. E. and Jontes, J. D. (2014). Protocadherin-18b interacts with Nap1 to control motor axon growth and arborization in zebrafish. *Mol. Biol. Cell* **25**, 633-642. doi:10.1091/mbc.e13-08-0475

Bosze, B., Ono, Y., Mattes, B., Sinner, C., Gourain, V., Thumberger, T., Tlili, S., Wittbrodt, J., Saunders, T. E., Strähle, U. et al. (2020). Pcdh18a regulates endocytosis of E-cadherin during axial mesoderm development in zebrafish. *Histochem. Cell Biol.* **154**, 463-480. doi:10.1007/s00418-020-01887-5

Chen, X., Koh, E., Yoder, M. and Gumbiner, B. M. (2009). A protocadherin-cadherin-FLRT3 complex controls cell adhesion and morphogenesis. *PLoS One* **4**, e8411. doi:10.1371/journal.pone.0008411

Chen, B., Brinkmann, K., Chen, Z., Pak, C. W., Liao, Y., Shi, S., Henry, L., Grishin, N. V., Bogdan, S. and Rosen, M. K. (2014). The WAVE regulatory complex links diverse receptors to the actin cytoskeleton. *Cell* **156**, 195-207. doi:10.1016/j.cell.2013.11.048

Chi, N. C., Shaw, R. M., De Val, S., Kang, G., Jan, L. Y., Black, B. L. and Stainier, D. Y. R. (2008). Foxn4 directly regulates tbx2b expression and atrioventricular canal formation. *Genes Dev.* **22**, 734-739. doi:10.1101/gad.1629408

Clark, A. G. and Vignjevic, D. M. (2015). Modes of cancer cell invasion and the role of the microenvironment. *Curr. Opin. Cell Biol.* **36**, 13-22. doi:10.1016/j.ceb.2015.06.004

Gao, X., Xu, C., Asada, N. and Frenette, P. S. (2018). The hematopoietic stem cell niche: from embryo to adult. *Development* **145**, dev139691. doi:10.1242/dev.139691

Harrison, O. J., Brasch, J., Katsamba, P. S., Ahlsen, G., Noble, A. J., Dan, H., Sampogna, R. V., Potter, C. S., Carragher, B., Honig, B. et al. (2020). Family-wide structural and biophysical analysis of binding interactions among non-clustered δ-protocadherins. *Cell Rep.* **30**, 2655-2671.e7. doi:10.1016/j.celrep.2020.02.003

Hayashi, S., Inoue, Y., Kiyonari, H., Abe, T., Misaki, K., Moriguchi, H., Tanaka, Y. and Takeichi, M. (2014). Protocadherin-17 mediates collective axon extension by recruiting actin regulator complexes to interaxonal contacts. *Dev. Cell* **30**, 673-687. doi:10.1016/j.devcel.2014.07.015

Helker, C. S. M., Schuermann, A., Karpanen, T., Zeuschner, D., Belting, H.-G., Affolter, M., Schulte-Merker, S. and Herzog, W. (2013). The zebrafish common cardinal veins develop by a novel mechanism: lumen ensheathment. *Development* **140**, 2776-2786. doi:10.1242/dev.091876

Herbomel, P. and Levraud, J. P. (2005). Imaging early macrophage differentiation, migration, and behaviors in live zebrafish embryos. *Methods Mol. Med.* **105**, 199-214. doi:10.1385/1-59259-826-9:199

Homayouni, R., Rice, D. S. and Curran, T. (2001). Disabled-1 interacts with a novel developmentally regulated protocadherin. *Biochem. Biophys. Res. Commun.* **289**, 539-547. doi:10.1006/bbrc.2001.5998

Jontes, J. D. (2016). The nonclustered protocadherins. In *The Cadherin Superfamily: Key Regulators of Animal Development and Physiology* (ed. S. T. Suzuki and S. H. Hirano), pp. 223-249. Springer.

Kimmel, C. B., Ballard, W. W., Kimmel, S. R., Ullmann, B. and Schilling, T. F. (1995). Stages of embryonic development of the zebrafish. *Dev. Dyn.* **203**, 253-310. doi:10.1002/aja.1002030302

Kissa, K., Murayama, E., Zapata, A., Cortes, A., Perret, E., Machu, C. and Herbomel, P. (2008). Live imaging of emerging hematopoietic stem cells and early thymus colonization. *Blood* **111**, 1147-1156. doi:10.1182/blood-2007-07-099499

Komoriya, A., Green, L. J., Mervic, M., Yamada, S. S., Yamada, K. M. and Humphries, M. J. (1991). The minimal essential sequence for a major cell type-specific adhesion site (CS1) within the alternatively spliced type III connecting segment domain of fibronectin is leucine-aspartic acid-valine. *J. Biol. Chem.* **266**, 15075-15079. doi:10.1016/S0021-9258(18)98588-1

Kraft, B., Berger, C. D., Wallkamm, V., Steinbeisser, H. and Wedlich, D. (2012). Wnt-11 and Fz7 reduce cell adhesion in convergent extension by sequestration of PAPC and C-cadherin. *J. Cell Biol.* **198**, 695-709. doi:10.1083/jcb.201110076

Le Guyader, D., Redd, M. J., Colucci-Guyon, E., Murayama, E., Kissa, K., Briolat, V., Mordelet, E., Zapata, A., Shinomiya, H. and Herbomel, P. (2008). Origins and unconventional behavior of neutrophils in developing zebrafish. *Blood* **111**, 132-141. doi:10.1182/blood-2007-06-095398

Lee, R. T. H., Knapik, E. W., Thiery, J. P. and Carney, T. J. (2013). An exclusively mesodermal origin of fin mesenchyme demonstrates that zebrafish trunk neural crest does not generate ectomesenchyme. *Development* **140**, 2923-2932. doi:10.1242/dev.093534

Morishita, H. and Yagi, T. (2007). Protocadherin family: diversity, structure, and function. *Curr. Opin. Cell Biol.* **19**, 584-592. doi:10.1016/j.ceb.2007.09.006

Murayama, E., Kissa, K., Zapata, A., Mordelet, E., Briolat, V., Lin, H.-F., Handin, R. I. and Herbomel, P. (2006). Tracing hematopoietic precursor migration to successive hematopoietic organs during zebrafish development. *Immunity* **25**, 963-975. doi:10.1016/j.immuni.2006.10.015

Murayama, E., Sarris, M., Redd, M., Le Guyader, D., Vivier, C., Horsley, W., Trede, N. and Herbomel, P. (2015). NACA deficiency reveals the crucial role of somite-derived stromal cells in haematopoietic niche formation. *Nat. Commun.* **6**, 8375. doi:10.1038/ncomms9375

Nakao, S., Platek, A., Hirano, S. and Takeichi, M. (2008). Contact-dependent promotion of cell migration by the OL-protocadherin-Nap1 interaction. *J. Cell Biol.* **182**, 395-410. doi:10.1083/jcb.200802069

Pancho, A., Aerts, T., Mitsogiannis, M. D. and Seuntjens, E. (2020). Protocadherins at the Crossroad of Signaling Pathways. *Front. Mol. Neurosci.* **13**, 117. doi:10.3389/fnmol.2020.00117

Parinov, S., Kondrichin, I., Korzh, V. and Emelyanov, A. (2004). Tol2 transposon-mediated enhancer trap to identify developmentally regulated zebrafish genes in vivo. *Dev. Dyn.* **231**, 449-459. doi:10.1002/dvdy.20157

Plaster, N., Sonntag, C., Busse, C. E. and Hammerschmidt, M. (2006). p53 deficiency rescues apoptosis and differentiation of multiple cell types in zebrafish *flathead* mutants deficient for zygotic DNA polymerase ∂1. *Cell Death Differ.* **13**, 223-235. doi:10.1038/sj.cdd.4401747

Redies, C., Vanhalst, K. and Van Roy, F. (2005). δ-Protocadherins: unique structures and functions. *Cell. Mol. Life Sci.* **62**, 2840-2852. doi:10.1007/s00018-005-5320-z

Robu, M., Larson, J. D., Nasevicius, A., Beiraghi, S., Brenner, C., Farber, S. A. and Ekker, S. C. (2007). p53 activation by knockdown technologies. *PLoS Genet.* **3**, e78. doi:10.1371/journal.pgen.0030078

Seger, C., Hargrave, M., Wang, X., Chai, R. J., Elworthy, S. and Ingham, P. W. (2011). Analysis of Pax7 expressing myogenic cells in zebrafish muscle development, injury, and models of disease. *Dev. Dyn.* **240**, 2440-2451. doi:10.1002/dvdy.22745

Stickney, H. L., Barresi, M. J. F. and Devoto, S. H. (2000). Somite development in zebrafish. *Dev. Dyn.* **219**, 287-303. doi:10.1002/1097-0177(2000)9999:9999<::AID-DVDY1065>3.0.CO;2-A

Suster, M. L., Abe, G., Schouw, A. and Kawakami, K. (2011). Transposon-mediated BAC transgenesis in zebrafish. *Nat. Protoc.* **6**, 1998-2021. doi:10.1038/nprot.2011.416

Tai, K., Kubota, M., Shiono, K., Tokutsu, H. and Suzuki, S. T. (2010). Adhesion properties and retinofugal expression of chicken protocadherin-19. *Brain Res.* **1344**, 13-24. doi:10.1016/j.brainres.2010.04.065

Thisse, C. and Thisse, B. (2008). High-resolution in situ hybridization to whole-mount zebrafish embryos. *Nat. Protoc.* **3**, 59-69. doi:10.1038/nprot.2007.514

Urbančič, V., Butler, R., Richier, B., Peter, M., Mason, J., Livesey, F. J., Holt, C. E. and Gallop, J. L. (2017). Filopodyan: an open-source pipeline for the analysis of filopodia. *J. Cell Biol.* **216**, 3405-3422. doi:10.1083/jcb.201705113

Vanhalst, K., Kools, P., Staes, K., Van Roy, F. and Redies, C. (2005). δ-Protocadherins: a gene family expressed differentially in the mouse brain. *Cell. Mol. Life Sci.* **62**, 1247-1259. doi:10.1007/s00018-005-5021-7

Wakayama, Y., Fukuhara, S., Ando, K., Matsuda, M. and Mochizuki, N. (2015). Cdc42 mediates Bmp - Induced sprouting angiogenesis through Fmnl3-driven assembly of endothelial filopodia in zebrafish. *Dev. Cell* **32**, 109-122. doi:10.1016/j.devcel.2014.11.024

Wolf, K., Mazo, I., Leung, H., Engelke, K., Von Andrian, U. H., Deryugina, E. I., Strongin, A. Y., Bröcker, E.-B. and Friedl, P. (2003). Compensation mechanism in tumor cell migration: Mesenchymal-amoeboid transition after blocking of pericellular proteolysis. *J. Cell Biol.* **160**, 267-277. doi:10.1083/jcb.200209006

Wu, J.-S., Jiang, J., Chen, B.-J., Wang, K., Tang, Y.-L. and Liang, X.-H. (2021). Plasticity of cancer cell invasion: Patterns and mechanisms. *Transl. Oncol.* **14**, 100899. doi:10.1016/j.tranon.2020.100899

Xue, Y., Liu, D., Cui, G., Ding, Y., Ai, D., Gao, S., Zhang, Y., Suo, S., Wang, X., Lv, P. et al. (2019). A 3D atlas of hematopoietic stem and progenitor cell expansion by multi-dimensional RNA-seq analysis. *Cell Rep.* **27**, 1567-1578.e5. doi:10.1016/j.celrep.2019.04.030